Quaternary Science Reviews 273 (2021) 107250

Contents lists available at ScienceDirect

Quaternary Science Reviews

journal homepage: www.elsevier.com/locate/quascirev

Seasonal variability in temperature trends and atmospheric circulation systems during the Eemian (Last Interglacial) based on *n*-alkanes hydrogen isotopes from Northern Finland

Christos Katrantsiotis [a, *], Elin Norström [b], Rienk H. Smittenberg [c], J. Sakari Salonen [d], Anna Plikk [e], Karin Helmens [f, g]

[a] Environmental Archaeology Laboratory, Department of Historical, Philosophical and Religious Studies, Umeå University, SE, 901 87 Umeå, Sweden
[b] Department of Physical Geography and the Bolin Centre for Climate Research, Stockholm University, 106 91, Stockholm, Sweden
[c] Department of Geological Sciences and the Bolin Centre for Climate Research, Stockholm University, 10691, Stockholm, Sweden
[d] Department of Geosciences and Geography, P.O. Box 64, 00014, University of Helsinki, Finland
[e] The Archaeologists, National Historical Museums, SE, 126 53, Hägersten, Sweden
[f] Swedish Museum of Natural History, P.O. Box 50007, 10405, Stockholm, Sweden
[g] Värriö Research Station, Institute for Atmospheric and Earth System Research INAR / Physics, P.O. Box 64, 00014, University of Helsinki, Finland

ARTICLE INFO

Article history:
Received 24 March 2021
Received in revised form
1 October 2021
Accepted 19 October 2021
Available online xxx

Handling Editor: Yan Zhao

Keywords:
Eemian
MIS 5e
Last Interglacial
Biomarkers
Hydrogen isotopes
Climate variability
Seasonality changes
Finland

ABSTRACT

The Last Interglacial warm period, the Eemian (ca. 130–116 thousand years ago), serves as a reference for projected future climate in a warmer world. However, there is a limited understanding of the seasonal characteristics of interglacial climate dynamics, especially in high latitude regions. In this study, we aim to provide new insights into seasonal trends in temperature and moisture source location, linked to shifts in atmospheric circulation patterns, for northern Fennoscandia during the Eemian. Our study is based on the distribution and stable hydrogen isotope composition (δD) of *n*-alkanes in a lake sediment sequence from the Sokli paleolake in NE Finland, placed in a multi-proxy framework. The δD values of predominantly macrophyte-derived mid-chain *n*-alkanes are interpreted to reflect lake water δD variability influenced by winter precipitation δD (δD_{prec}), ice cover duration and deuterium (D)-depleted meltwater. The δD values of terrestrial plant-derived long-chain *n*-alkanes primarily reflect soil water δD variability modulated by summer δD_{prec} and by the evaporative enrichment of soil and leaf water. The δD_{prec} variability in our study area is mostly attributed to the temperature effect and the moisture source location linked to the relative dominance between D-depleted continental and polar air masses and D-enriched North Atlantic air masses. The biomarker signal further corroborates earlier diatom-based studies and pollen-inferred January and July temperature reconstructions from the same sediment sequence. Three phases of climatic changes can be identified that generally follow the secular variations in seasonal insolation: (i) an early warming trend succeeded by a period of strong seasonality (ii) a mid-optimum phase with gradually decreased seasonality and cooler summers, and (iii) a late climatic instability with a cooling trend. Superimposed on this trend, two abrupt cooling events occur in the early and late Eemian. The Sokli δD variability is generally in good agreement with other North Atlantic and Siberian records, reflecting major changes in the atmospheric circulation patterns during the Eemian as a response to orbital and oceanic forcings.

1. Introduction

Earth has warmed by about 0.9–1 °C over the past century while the Arctic has experienced a warming of 2–3 °C over the same period (IPCC, 2018, 2021). Most recent projections indicate that global warming will reach 1.5 °C by 2030, if temperature continues to increase at the current rate (IPCC, 2021). Global warming has

* Corresponding author.
E-mail addresses: christos.katrantsiotis@umu.se (C. Katrantsiotis), Elin.Norstrom@natgeo.su.se (E. Norström), rienk.smittenberg@geo.su.se (R.H. Smittenberg), sakari.salonen@helsinki.fi (J.S. Salonen), Anna.Plikk@arkeologerna.com (A. Plikk), Karin.Helmens@nrm.se (K. Helmens).

https://doi.org/10.1016/j.quascirev.2021.107250

been attributed to anthropogenic greenhouse forcing, though superimposed on the natural climate variability. More knowledge of past climate is, therefore, required (i) to understand the nature and rate of current climate change, (ii) to distinguish anthropogenic effects, and further (iii) to accurately project climate system responses to future changes (Jansen et al., 2007).

The Quaternary has been characterized by cold glacial and warm interglacials periods paced by cyclical changes in Earth's orbital parameters (Tzedakis et al., 1997; Maslin, 2009). Of these periods, the Eemian (Last Interglacial, Marine Isotope Stage (MIS) 5e, ca 130–116 ka) is of special interest as it represents the most recent interval of widespread climatic warming in the geologic records with global mean temperatures of ca. 0.8 °C above preindustrial levels (Fischer et al., 2018). Although the magnitude of warming and the underlying forcing mechanisms were different during the Eemian (orbital) compared to the modern/industrial era (anthropogenic greenhouse effects), both periods are characterized by a similar latitudinal temperature distribution with an amplified warming in the northern high-latitudes. This has been attributed to various feedback mechanisms, mainly the surface albedo feedback (Schurgers et al., 2007). It has been estimated that the Circum-Arctic area experienced summer temperatures of 4–10 °C higher than present during the Eemian (CAPE-Last Interglacial Project Members, 2006; Francis et al., 2006; Landais et al., 2006). Thus, the Eemian is considered as a reference for climate model validation outside of near-present-day conditions and for studying the strength of positive feedback mechanisms and the response of environments to a warmer-than-present world (MacCracken and Kutzbach, 1991; Bakker et al., 2014; Pedersen et al., 2016).

In order to use the Eemian as a suitable analogue for testing future climate hypotheses, a better understanding of climate dynamics prevailing during this period is required. Large efforts have been made towards this direction by establishing networks of spatially distributed high-resolution proxy records (e.g. Field et al., 1994; Drysdale et al., 2005; Helmens et al., 2015; Demény et al., 2017; Finné et al., 2019; Wilcox et al., 2020). However, Eemian climate synthesis is still impeded by temporally and spatially fragmented data. Speleothem studies are of high resolution, but they often cover limited time periods due to hiatuses (Finné et al., 2019). In addition, Eemian sediment records are scarce from high northern latitude regions (60–90°N) (Helmens, 2014; Curtin et al., 2019) because of the subsequent glacial erosion. Therefore, there are still large uncertainties regarding the regional patterns and drivers of the Eemian climate trends (Galaasen et al., 2014; Salonen et al., 2018; Tzedakis et al., 2018), along with highly uncertain climate modelling especially for the winters (Bakker et al., 2013).

The Sokli basin in NE Finland is one of the few high-latitude continental sites where a complete Eemian sediment sequence with an unequivocal age has been preserved under last glacial (Weichselian) and Holocene sediments (Helmens et al., 2007; Plikk et al., 2016). The basin constitutes a steep depression in deeply weathered rock of a Paleozoic magma intrusion. In this depression, sediments have been protected from glacial erosion and are further preserved in their original stratigraphic position near the central area of Fennoscandian glaciations (Helmens et al., 2015).

In 2010, a continuous Eemian sediment sequence was retrieved from Sokli and it has been the focus of multi-proxy studies including pollen, plant macrofossils, diatoms and chironomids (Helmens et al., 2015; Plikk et al., 2016, 2019·bib_Plikk_et_al_2016; Salonen et al., 2018·bib_Plikk_et_al_2019). In this study, we utilize lipid biomarkers to gain an even more comprehensive insight into the paleo-environmental and paleoclimatic history of the Sokli site. In particular, we focus on the hydrogen isotope composition (δD) of *n*-alkanes, an established proxy in paleoclimate research (e.g. Sachs et al., 2009; Aichner et al., 2015; Katrantsiotis et al., 2019; Goldsmith et al., 2019; McFarlin et al., 2019). The δD signal of macrophyte-derived mid-chain *n*-alkanes (δD_{aq}) reflects the lake water δD (δD_{lake}) variability, which in the region of northern Fennoscandia has been shown to be largely biased towards winter precipitation δD (δD_{prec}) during prolonged periods of ice cover and late snowmelt (Jonsson et al., 2009). In contrast, soil water used by terrestrial plants is mostly recharged by summer rainfall, and therefore, δD of terrestrial plant-derived *n*-alkanes (δD_{terr}) predominantly reflects summer δD_{prec} variability enhanced by the evaporative enrichment of soil and leaf water (Kahmen et al., 2013; Throckmorton et al., 2016). In this region, the δD_{prec} signal is modulated by air temperature and moisture source, associated with the relative dominance of D-depleted air masses from north/northeast and D-enriched air masses from west/southwest (Dansgaard, 1964; Rosqvist et al., 2004). Therefore, the biomarker δD approach offers the possibility to extract information about seasonal variations in the sub-Arctic temperature and moisture source associated with shifts in the atmospheric circulation patterns over the Eemian.

The specific goals of this study are: (i) to reconstruct seasonal variations in temperature trends and moisture source location in northern Fennoscandia during the Eemian, (ii) to evaluate these data through comparison with previously published records from the same core and also other regional studies, and (iii) to understand the Eemian climate dynamics by exploring the role of large-scale atmospheric circulation patterns behind the observed variability. By doing so, we can improve our understanding of the atmospheric mechanisms affecting the sub-arctic climate in a warmer world.

2. Regional climate and atmospheric circulation patterns

Finland encompasses various climatic zones ranging from temperate in the south, continental/subarctic in the east to maritime/subarctic in the west and north, with strong seasonal contrasts and high spatial heterogeneity (Kortelainen and Karhu, 2004). Mean annual precipitation varies from 651 to 700 mm in southern and central Finland to less than 550 mm along the west coast and in the northern part with the highest amount of precipitation occurring during summer (ca. 209 mm) (Irannezhad et al., 2016). Mean annual temperature varies from +5 °C in the south to −3 °C in the north with seasonal temperature means ranging from −12.5 to −2.0 °C in winter and from 7.0 to 16.1 °C in summer (Irannezhad et al., 2015). An increasing trend in precipitation by 0.92 ± 0.50 mm $year^{-1}$ from 1901 to 2011 and temperature by 0.4 ± 0.2 °C per decade for same period has been observed, especially in northern Finland (0.50–0.58 °C per decade) during winter and spring (Irannezhad et al., 2015).

Climatic conditions in Finland are largely influenced by the interplay between various large-scale atmospheric circulation patterns associated with the Arctic, North Atlantic and Siberia (Fig. 1) (Autio and Heikkinen, 2002). The Arctic Oscillation (AO) indicates the strength of circumpolar vortex and is the most influential atmospheric circulation pattern in winter and spring temperatures in Finland (Järvenoja, 2005; Irannezhad et al., 2015). The North Atlantic Oscillation (NAO) index describes the intensity of the westerly airflow from the North Atlantic to the Atlantic European sector. It generally shows a weaker correlation with the annual and winter temperature in Finland compared to the AO but stronger with winter precipitation (Irannezhad et al., 2014, 2015). Positive AO and NAO phases correspond to the strengthening of the westerly circulation and the dominance of mild and moist, maritime airflow over northern Europe (Lee et al., 2020). Persistent cold easterly airflow can be caused by the Siberian High, a surface high-pressure system that covers large portions of the Eurasian

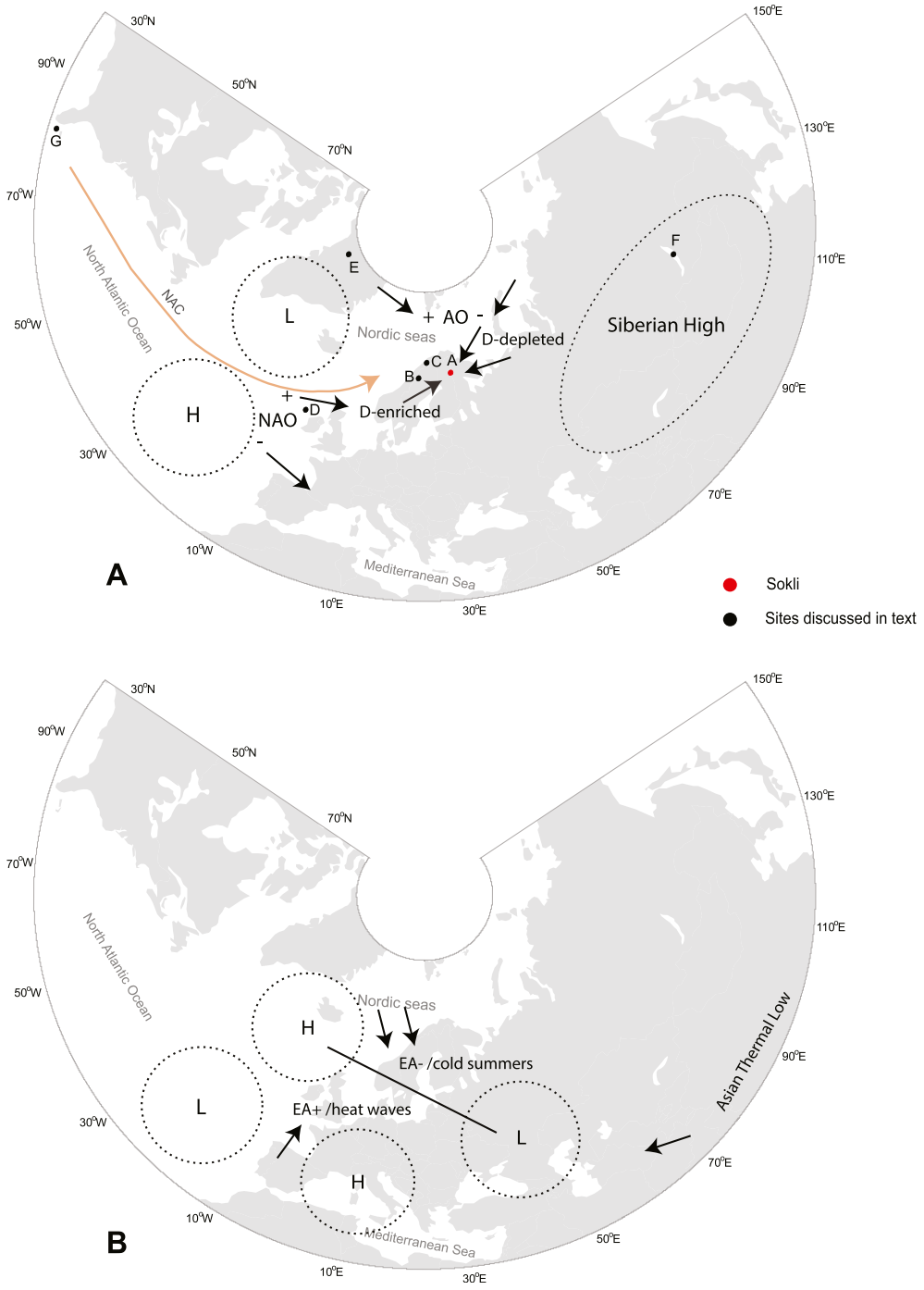

Fig. 1. (A) Major winter atmospheric circulation patterns affecting Scandinavia climate dynamics (see also paragraph 2). NAO - North Atlantic Oscillation, AO - Arctic Oscillation, H - High pressure system, L- Low pressure system. (B) Atmospheric circulation patterns over Europe during summers with the effects of EA (East Atlantic) atmospheric pattern. Paleoclimatic records discussed in the text and plotted in Fig. 8: A-Sokli, B- Korallgrottan Cave, C- Okshola Cave, D-Ocean Drilling Program ODP Site 980, E-NEEM, F-Lake Baikal, G-MD99-2202 site in the Bahamian archipelago.

continent and strengthens during negative AO phases (Huang et al., 2016). The East Atlantic/West Russia pattern (EA/WR) is associated with the westward ridging of the Siberian High mainly affecting the late winter, spring and autumn temperatures and precipitation (Ionita, 2014; Irannezhad et al., 2015). Summer temperatures in Finland are mostly influenced by the East Atlantic (EA) atmospheric pattern, a well-defined dipole at 500-hPa geopotential height with action centers over the North Atlantic and the Eastern Europe region (Fig. 1) (Wallace and Gutzler, 1981; Irannezhad et al., 2015; Mikhailova and Yurovsky, 2016). Positive (negative) EA phases are associated with a southerly (northerly) airflow leading to above (below)-average summer temperatures (Wulff et al., 2017).

3. Study site

The Sokli site (67°48′ N 29°18′ E, 220 m a.s.l.) is located in eastern Finnish Lapland, NE Finland, close to the Russian border (Fig. 2). The underlying bedrock consists of deeply weathered rocks

of Palaeozoic carbonate-rich magma intrusion called the Sokli Carbonatite Massif that penetrates through the crystalline Precambrian shield (Vartiainen, 1980). The massif forms a circular basin of ca. 5 km in diameter and is surrounded by gently sloping hills reaching up to ca. 320 m a.s.l. The massif is crossed by a NE-SW trending fracture zone along which smaller sedimentation basins have been formed (Talvitie et al., 1981). The Sokli basin (ca. 2 km^2) is located in the center of massif and is covered by 10–30 m of Late Quaternary deposits and ca. 2 m of Holocene peat that forms the present-day mire. A small stream (Soklioja) crosses the mire entering from the NE and draining towards the SW (Fig. 2).

The regional vegetation is boreal forest dominated by birch (*Betula pubescens* and *B. pendula*) and spruce (*Picea abies*) on the lower slopes around mire and pine (*Pinus sylvestris*) in the upper slopes and summits (Helmens et al., 2000). Wetland vegetation includes white mosses (*Sphagnum*), cloudberry (*Rubus chamaemorus*), Ericaceae, dwarf birch (*Betula nana*), willows (*Salix*) and sedges (*Carex*) (Helmens et al., 2000). The highest peaks (ca. 500 m a.s.l.) are located at ca. 20 km SE of Sokli, above the altitudinal treeline, and are covered with shrub tundra. Present climate is cold boreal with mean annual temperature of −1 °C and mean July and February temperatures of 13 °C and −14 °C, respectively (Irannezhad et al., 2016). Annual precipitation ranges between 500 and 550 mm; summer precipitation is ca. 140–160 mm/season and winter precipitation ca. 100–120 mm/season (Irannezhad et al., 2014). The lakes around Sokli are covered by ice between October and May (Plikk et al., 2019).

4. Methods

4.1. Sediment coring, stratigraphy and chronology

A sediment sequence of 12 m was retrieved from the Sokli paleolake in the winter of 2010 by the Geological Survey of Finland using percussion drilling with a flow-through coring device. The sequence contains 3 m of glacio-lacustrine sands between 25 m and 28 m and 9 m of diatom gyttja between 16 m and 25 m, laminated in the lower part and intercalated with sand/gravel layers near the top. More details about the coring and sub-sampling can be found in Plikk et al. (2016).

The diatom gyttja layer with its yellowish-brown color stretches as a marker horizon through the Sokli basin near the bottom of the late Quaternary basin infill. Its interglacial pollen flora was first noted by Ilvonen (1973) and correlated to the Eemian Interglacial. This age assignment was later supported by stratigraphic studies on the overlying Weichselian sequence, combined with optically stimulated luminescence (OSL), thermoluminescence (TL) and infrared stimulated luminescence (IRSL) dating of underlying and overlying sands providing an age of between 180–150 and 110–95 ka BP (Helmens et al., 2000, 2007; Alexanderson et al., 2008). In the present study, we use the age-depth model for the Eemian diatom gyttja bed as presented by Salonen et al. (2018) in order to facilitate a large-scale comparison of our results with other regional paleoclimate datasets and climate forcing time series. In this model, the onset and end of interglacial conditions are based on the

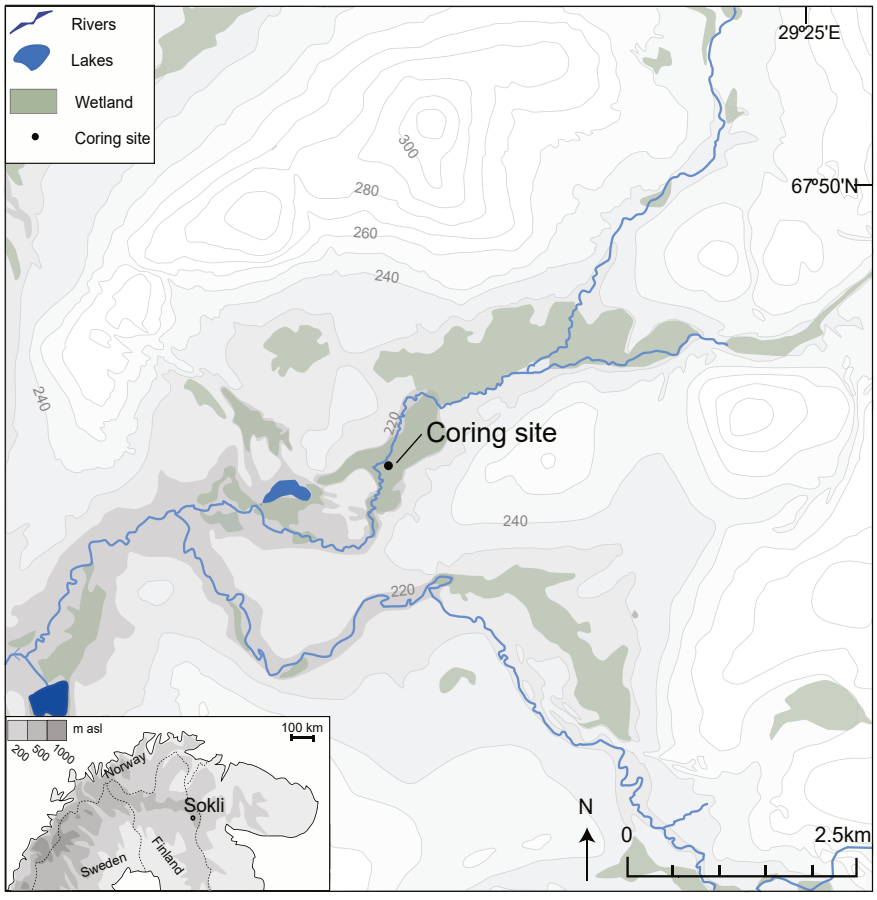

Fig. 2. Topographical map of the Sokli site and the surrounding area, with the location of the coring site (simplified after Plikk et al., 2016).

correlation between the pollen-based temperature reconstruction at Sokli and stalagmites records from northern Sweden, Belgium and the Alps (Salonen et al., 2018 and references therein). The model uses an age of 130.9 ± 1 ka BP (2σ error; at sediment depth of 25.17 m) at the onset and an age of 117.5 ± 0.5 ka BP (1585 cm) at the end of the Eemian interglacial conditions at Sokli and assumes constant sedimentation between the dates (supplementary material; Salonen et al., 2018). Uncertainties are estimated to be higher in the Mid-Eemian, reaching 2σ values of ca. 1500 years (Salonen et al., 2018).

4.2. Bulk geochemical analysis

A total of 60 samples, covering a depth interval of 2–4 cm each, were taken from the diatom gyttja and the uppermost part of the underlying glacio-lacustrine sand (subsampling depth: 2515–1630 cm). The samples were freeze-dried and homogenized with an agate pestle and porcelain mortar for total organic carbon (TOC), total nitrogen (TN) and stable carbon isotope ($\delta^{13}C_{org}$) analyses. Approximately 10 mg of each sample were weighed and placed into tin capsules. The samples were acidified with 1.5 M HCl to remove carbonates and dried at 60 °C overnight. TOC, TN and $\delta^{13}C_{org}$ were quantified with a Carlo Erba NC2500 elemental analyzer coupled with a Finnigan MAT Delta V mass spectrometer at the Stable Isotope Laboratory, Stockholm University. The TOC and TN values are expressed as % with a relative error <1%. These values were used to calculate the C/N ratio. The $\delta^{13}C$ values are expressed in per mil relative to Vienna Pee-Dee Belemnite with an analytical error of ±0.15‰.

4.3. n-alkane extraction, identification and quantification

Total lipid extracts were obtained via sonication of ca. 10–15 g of freeze-dried and powdered sediment samples (Katrantsiotis et al., 2018). The samples were mixed with dichloromethane and methanol (DCM–MeOH, 9:1, v/v), placed in a sonic bath for ca. 20 min and centrifuged at 3000 rpm. This extraction procedure was repeated three times. The extracts were combined into a total lipid extract, then separated into fractions of different polarity using silica-based solid-phase extraction. Apolar fractions were obtained using *n*-hexane as eluent; from these fractions saturated hydrocarbon fractions were obtained by a second elution with *n*-hexane over pipette columns (3x column volume) filled with glass wool, activated copper to remove elemental Sulphur, and 10% AgNO3-coated silica gel.

The hydrocarbon fractions were analyzed by gas chromatography–mass spectrometry (Shimadzu-QP2010 Ultra system), for *n*-alkane identification and quantification. The system was equipped with an AOC-20i auto sampler and a split-splitless injector operated in splitless mode. A Zebron ZB-5HT Inferno GC column (30m × 0.25mm × 0.25 μm) was used for compound separation. The GC oven temperature was programmed from 60 °C to 180 °C at a rate of 20 °C/min followed by a rate of 4 °C/min until 320 °C where it was held for 20 min. Quantification was performed with an external calibration curve, produced by analyzing regularly a *n*-C_{21-40} alkane standard solution (Fluka Analytical) at different concentrations. The GC-MS Solution software 4.11 (Shimadzu) was used for compound identification and area integration of the relevant peaks. The *n*-alkane relative abundances were calculated by dividing the peak areas of each homologue (C_n where n ranges from 23 to 31) with the sum of all peak areas (Σ C_{23-31}). The carbon preference index (CPI) was calculated as: $CPI = \Sigma_{odd}/\Sigma_{even}$ (Wang et al., 2003). The average chain length (ACL) was determined as: $ACL = \Sigma (n * C_n)/\Sigma C_n$ where Cn is the concentration (mgg^{-1} dry weight) of odd chain *n*-alkanes (Tanner et al., 2010).

4.4. n-alkanes δD

The stable hydrogen isotopic composition (deuterium/hydrogen ratio) of *n*-alkanes (δD) was analyzed using a Thermo gas chromatography-isotope ratio mass spectrometry (GC-IRMS) system,which consisted of a Trace Ultra GC connected to Delta V Ultra IRMS system via a GC-isolink and ConFlo IV system. The GC oven was programmed to increase at a rate of 15 °C/min from 100 °C to 250 °C followed by a rate of 10 °C/min until 320 °C, with a final hold time of 9 min. Two μl of each sample were injected into the GC. The inlet was operated in a splitless mode under pressure of 50 p.s.i. during 1.5 min. After the splitless time, pressure was reduced; the split flow of 100 ml/min was decreased to 40 ml/min after 5 min (gas saver mode). Helium was used as a carrier gas at constant flow mode. The compounds were separated in a Zebron ZB-5HT Inferno GC column (50 m × 0.250 mm × 0.25 μm). A reference standard of *n*-alkanes with known δD composition (reference mixture A6, provided by Arndt Schimmelmann, Indiana University, USA) was run several times daily between the samples (i) to calibrate the reference gas (H_2) against which the isotopic compositions were measured and (ii) to check instrument performance. The long-term precision was ca. 1.5‰. The H3+ factor was fairly stable with an average value of 3.9 ppm mV−1. All analyses were performed in triplicate or duplicate, yielding average standard deviations of 1.16‰ for *n*-C_{23}, 1.15‰ for *n*-C_{25}, 0.97‰ for *n*-C_{27}, 1.36‰ for *n*-C_{29} and 2.34‰ for *n*-C31. The isotopic values were calculated using ISODAT software and are reported as mean values relative to Vienna Standard Mean Ocean Water (VSMOW).

5. Results and interpretation

5.1. Bulk geochemistry

The TOC content shows shifts from ca. 1% in the lower minerogenic layer to ca. 10–13% in the diatom gyttja between 24.80 m and 16.30 m (Fig. 3). The C/N ratio shows an increase from ca. 9–10 to ca. 12–15 suggesting a shift from input of aquatic organic matter to an equally large input of terrestrial and aquatic organic matter within the organic rich layer (Meyers and Teranes, 2001). The $\delta^{13}C_{org}$ profile displays values at ca. −32‰ in the minerogenic layer with a continuous increase after 24.80 m reaching up to ca. −27‰ within the diatom gyttja where it reamins relatively stable. Planktonic algae usually have lower $\delta^{13}C_{org}$ values (−32 ± 3‰) than the benthic taxa (−26 ± 3‰) due to their thinner diffuse boundary layer (France, 1995). Therefore, the increasing $\delta^{13}C_{org}$ values are most likely influenced by the high abundance of benthic species within the diatom gyttja layer (Plikk et al., 2016).

5.2. Distribution and sources of n-alkanes

The *n*-alkane distribution is dominated by odd-carbon numbered compounds in the range of C_{23} to C_{31} showing abundances from 12 to 40% (Fig. 4). The *n*-C_{25} alkane shows the highest abundance and variability from 19% at the bottom to 36% in the diatom gyttja. High CPI values (>2) indicate the plant origin of *n*-alkanes (Bush and McInerney, 2013). Slight variations in the ACL index between 25 and 28 are related to shifts in the abundance of the mid- (C_{23}–C_{25}) and long-chain *n*-alkanes (C_{27}–C_{31}).

The *n*-C_{23} and *n*-C_{25} alkanes are normally synthesized from aquatic macrophytes and *Sphagnum* species (Ficken et al., 2000; Bush and McInerney, 2013). In the Sokli core, the most dominant macrophyte is *Myriophyllum spicatum*-type, which can produce *n*-alkanes with high concentration of *n*-C_{23} and *n*-C_{25} compounds (Liu and Liu, 2016). This plant mainly occurs between 24.60 m and 21.00 m exhibiting a similar pattern of variability as the *n*-C_{23} and

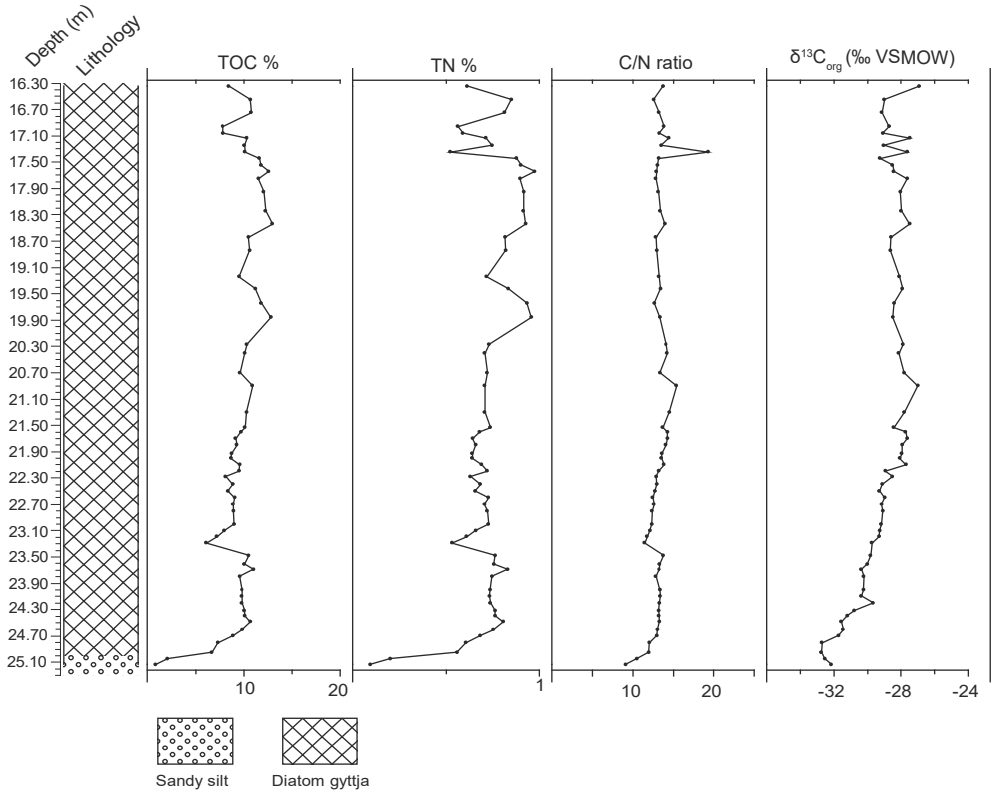

Fig. 3. Profile of the Sokli sequence showing the variation in the amount of TOC and TN content, the C/N ratio and the $\delta^{13}C_{org}$ values.

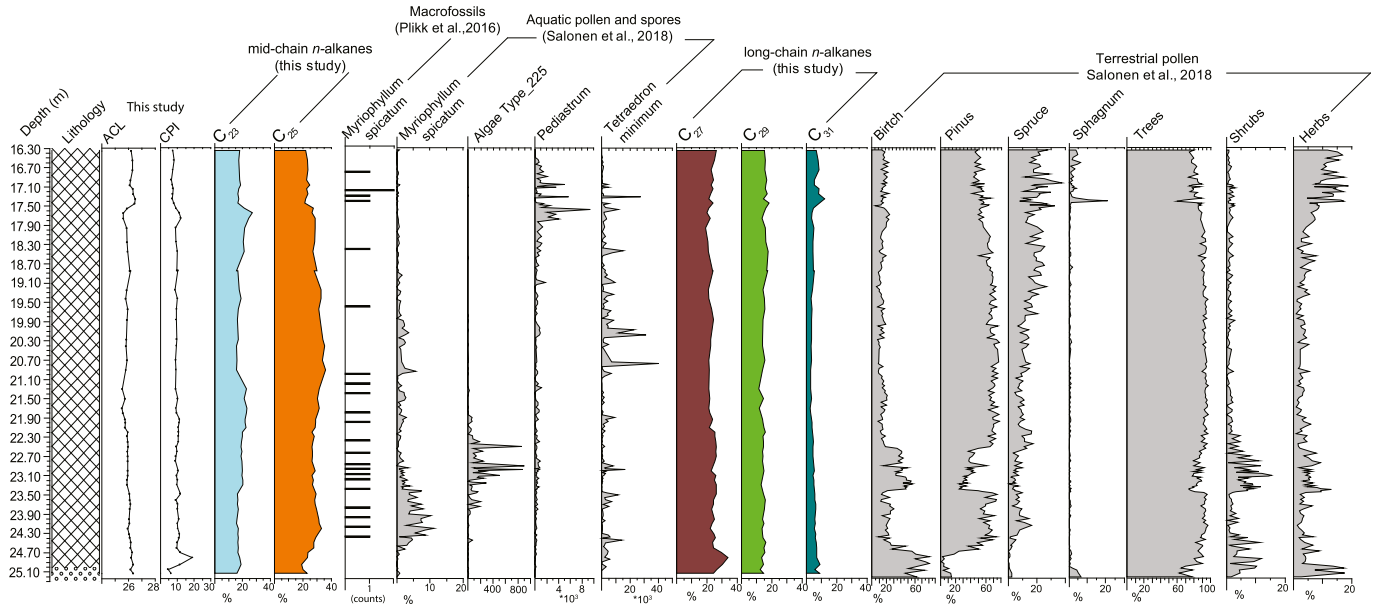

Fig. 4. Depth profiles of carbon preference index (CPI_{23-31}) and average chain length (ACL), relative abundances of mid-chain (aquatic) *n*-alkanes in comparison with selected pollen, spores and macrofossils of aquatic plants as well as relative abundances of long-chain (terrestrial) *n*-alkanes in comparison with the percentages of terrestrial plant functional groups in the Sokli core (after Salonen et al., 2018).

n-C_{25} alkanes (Fig. 4). In addition, the sequence contains a large amount of chlorophytes, e.g. algal type T.225, *Tetraëdron minimum* and *Pediastrum* spp., which can biosynthesize both short and long-chain *n*-alkanes maximizing at C_{10} and at C_{25-27} (Blokker et al., 1998). *Tetraëdron minimum* is one of the most abundant green algae in the record and is similarly distributed as *n*-C_{25} exhibiting higher percentages between 19 m and 20 m and a decreasing trend upwards (Fig. 4). It is thus likely that the mid-chain *n*-alkanes are

mostly derived from both green algae and *Myriophyllum spicatum* with proportionally larger contribution of these aquatic sources to *n*-C_{25}. *Sphagnum* species show a distinct increase at 17.40 m and, therefore, some contribution of peat mosses to mid-chain homologues is possible in this part of the sequence.

The long chain homologues, i.e. *n*-C_{27} to C $_{31}$ alkanes are usually derived from terrestrial vegetation (Rao et al., 2011; Bush and McInerney, 2013). The *n*-C_{27} and *n*-C_{29} alkanes are preferably synthesized by woody plants and shrubs while the *n*-C_{31} and *n*-C_{33} alkanes are produced by grasses and herbs (Zech et al., 2009; Bliedtner et al., 2018). In the Sokli core, the *n*-C_{27} and *n*-C_{29} alkanes likely have a common source as they both display relatively stable and high abundances and strong correlation ($r \approx 1$). These two homologues can be associated with arboreal plants i.e. *Pinus* (pine), *Betula* (birch) and *Picea* (spruce) as reflected in the pollen diagram (Fig. 4; Salonen et al., 2018). These plants are dominated by *n*-C_{27} and *n*-C_{29} alkanes with *Betula* producing higher concentrations of *n*-C_{27} (Diefendorf et al., 2011; Aichner et al., 2018). The *n*-C_{31} alkane exhibits a weak anti-correlation with *n*-C_{27} and *n*-C_{29} ($r \approx -0.1$) and displays high abundances below 14.80 m and above 17.30 m where herbs dominate the sequence. This suggests that the *n*-C_{31} alkane may derive from herbaceous plants, also reflected in the ACL, as higher values correspond to decreasing contribution of arboreal pollen and higher abundance of herbaceous pollen (Fig. 4). Therefore, shifts in ACL likely reflect changes between woody and herbaceous plants (Bliedtner et al., 2018 Aichner et al., 2018).

5.3. *n*-alkanes δD and precipitation δD (δD_{prec})

Compound-specific δD values of *n*-alkanes vary between −230‰ and −156‰ with *n*-C23 showing the highest variability, i.e. ca 74‰, compared to the other compounds (41‰ for *n*-C_{25}, 29‰ for *n*-C_{27}, 24‰ for *n*-C_{29} and 49‰ for *n*-C_{31}) (Fig. 5). Overall, the δD profiles of individual *n*-alkanes exhibit similar long-term trends ($r \approx 0.7$, $p < 0.05$), implying that they all record changes in the isotopic composition of source water, namely meteoric water that recharges soil and lake waters. These isotopic changes are predominantly driven by the temperature and moisture source effects (Dansgaard, 1964; Wang and Chen, 2020). In Finland, a strong correlation exists between δD_{prec} and mean annual temperature (Kortelainen and Karhu, 2004; Kyllönen, 2018) and monthly air surface temperature ($r \approx 0.8$, $p < 0.05$) whereas the amount effect has less influence on δD_{prec} ($r \approx 0.4$, $p < 0.05$) (Fig. 6; IAEA 2020; Rovaniemi station). In addition, different moisture sources have distinct δD signals: warm and moist air masses originating from the North Atlantic carry isotopically enriched vapor whereas cold and less moist continental air masses deriving from the Arctic and Siberia are characterized by isotopically depleted vapor (Jonsson et al., 2009; Theakstone, 2011; Bonne et al., 2020). Since compound-specific δD records the δD_{prec} variability, changes in the relative contributions of these air masses and, by inference, atmospheric circulation patterns, to local precipitation can be traced in *n*-alkanes δD. This signal can be further biased by the winter or summer δD variability of source water depending on the ice cover duration and meltwater inflow as well as the seasonality of photosynthesis and soil recharge in this subarctic region (Jonsson et al., 2009; Throckmorton et al., 2016; Thienemann, 2017).

5.3.1. Aquatic plant and algal-derived n-alkane δD (δD_{aq}) and lake water δD (δD_{lake})

The δD signature of lake water (δD_{lake}), recorded by δD of aquatic plant- and algal-derived mid-chain *n*-alkanes (δD_{aq}), is generally influenced by the balance between freshwater input and evaporation (Duan et al., 2011; Guenther et al., 2013). In this subarctic region, however, almost half of the annual precipitation falls as snow and lakes are characterized by prolonged ice cover. As a result, δD_{lake} in northern Fennoscandian lakes has been shown to be largely influenced by the ice cover duration and the timing of D-depleted snowmelt (winter δD_{prec}) with late snowmelt in spring/

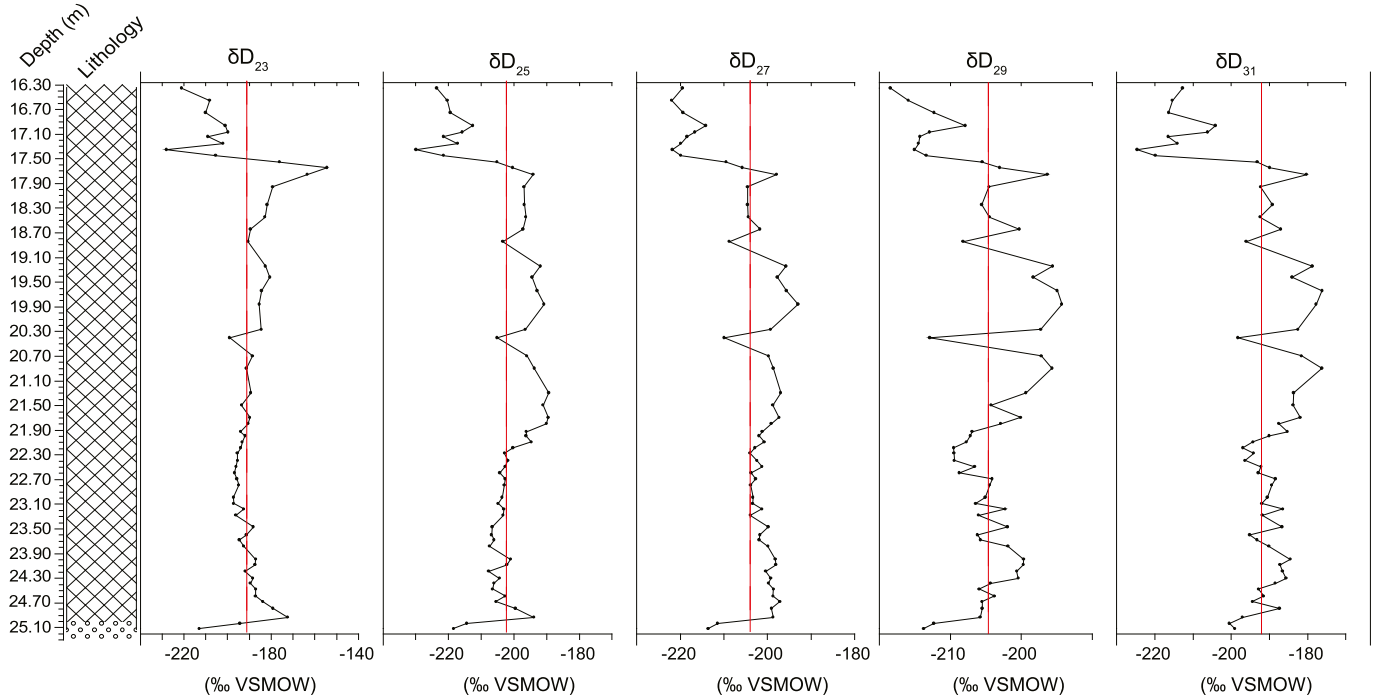

Fig. 5. Vertical profiles of the δD values of the individual *n*-alkanes with the red dashed lines showing the average values, expressed as ‰ against Vienna Standard Mean Ocean Water (VSMOW). (For interpretation of the references to colour in this figure legend, the reader is referred to the Web version of this article.)

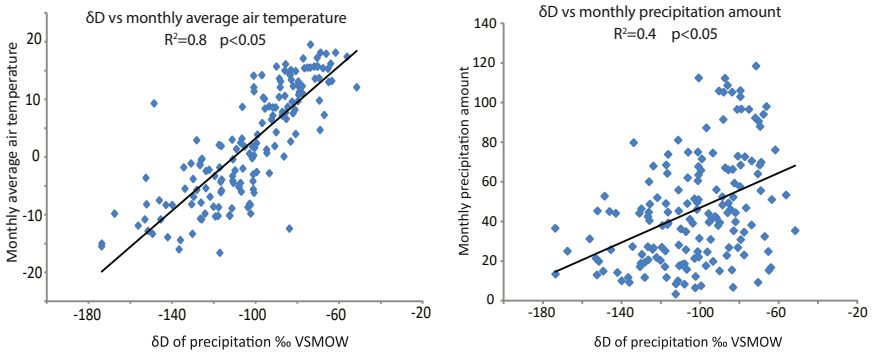

Fig. 6. Correlation plots between (a) δD of precipitation with the monthly average air temperature and (b) precipitation amount. All plots are based on data from Rovaniemi Station for the period between 2004 and 2019 (data from GNIP Database http://nucleus.iaea.org).

summer extending the period during which isotopically depleted snowmelt can influence δD_{lake} (Jonsson et al., 2009). This is especially a characteristic of lakes with higher catchment elevations and large inputs of recharge water that have been shown to be insignificantly affected by the evaporative isotopic enrichment and to retain water isotopic signal close to winter δD_{prec} (Jonsson et al., 2009). Similar topographical and climate settings also apply at the Sokli paleolake (Fig. 2); therefore, longer ice cover duration and later input of D-depleted snowmelt during periods of prolonged winters would diminish the relative contribution of summer precipitation and summer evaporation in δD_{lake}, leading to a greater preservation of the (low) winter signal in δD_{lake}. This interpretation is further consistent with the variability between δD_{aq} and the amount of nordic/alpine diatom flora in the Sokli Eemian sequence (compilation diagram of proxies in Fig. 7; δD_{aq} and Fragilariaceae). Lower δD_{aq} (represented by δD_{23}) values coincide with an increase in *Fragilaria* that are common in alpine and Arctic lakes and indicate prolonged, cold winters, with extensive ice cover and lower water depths (Fig. 7) (Paul et al., 2010; Plikk et al., 2016; Zalat et al., 2018). Therefore, we argue that δD_{aq} predominantly represents winter δD_{lake} variations influenced by δD_{prec}, the ice cover duration and the timing of D-depleted meltwater. Lower δD_{aq} values indicate cold periods dominated by D-depleted air masses from the Artic and/or Siberia, prolonged ice-cover seasons and late summer melting causing aquatic plants to incorporate the D-depleted lake water. Higher δD_{aq} values reflect warmer periods dominated by D-enriched moisture sourced from the North Atlantic and shorter ice-cover seasons causing plants to incorporate D-enriched lake water,

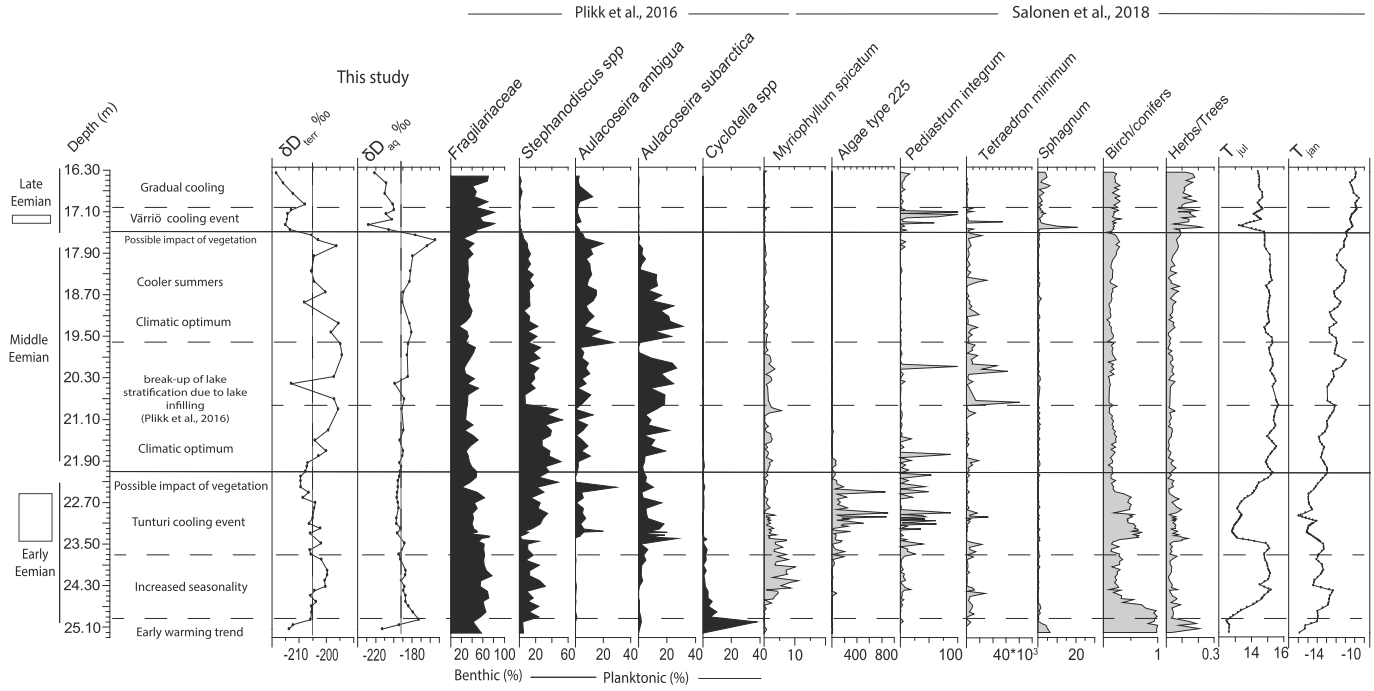

Fig. 7. Synthesis of proxy data in the Sokli core. δD_{terr} (δD_{29}) and δDaq (δD_{23}) records (this study). Most abundant diatom species (Plikk et al., 2016). Fragilariaceae percentage consists of the total sum of *Staurosira construens* var. *venter*, *S. construens* var. *construens*, *Staurosirella lapponica*, *S. leptostauron*, *S. pinnata*, and *Pseudostaurosira brevistriata*. *Stephanodiscus* spp includes the species *S. medius*, *S. parvus*, *S. minutulus*, *S. alpinus* and *Cyclotella* spp consists of the species *C. radiosa* and *C. michiganiana*. Pollen percentage of *Myriophyllum*,spores of selected green algae and *Sphagnum*, the ratio of total percentage of birch to conifers (*Pinus* and *Picea*), the ratio of total amount of herbs to total amount of trees and shrubs and the pollen based T_{jan} and T_{jul} reconstructions (Salonen et al., 2018). The record is divided into 3 phases representing the early, middle and late Eemian. Different climatic zones were identified based on the integration of δD_{terr} and δD_{aq}, the diatom and pollen data representing cold/dry and warm/wetter periods. The bars next to the depth scale indicate the Tunturi and Värriö cooling events as they were first defined by Helmens et al. (2015), Plikk et al. (2016) and Salonen et al. (2018).

possibly enhanced by higher evaporation rates under prolonged warm conditions.

5.3.2. Terrestrial leaf wax δD (δD_{terr})

In the sub-arctic regions, terrestrial plants mostly photosynthesize between May and September because of the temperature and light limitations during the rest of the year (Throckmorton et al., 2016). In addition, soil water utilized by the plants is mainly recharged by summer rainfall and is influenced by evaporative enrichment (Thienemann, 2017; Kjellman et al., 2020). Thawing of soils and snowmelt carrying the winter δD_{prec} signal likely contribute to a much lesser extent, as meltwater pulses quickly run off the landscape during spring and summer (Throckmorton et al., 2016). Therefore, δD of terrestrial plant-derived *n*-alkanes δD_{terr} (δD_{29}) reflects summer δD_{prec} variability, enhanced by the evaporative enrichment of soil and leaf water (Kjellman et al., 2020). This variability is further associated with changes in summer temperature and moisture source (Rosqvist et al., 2004). Lower δD_{terr} values indicate colder summers dominated by Arctic, D-depleted air masses, while higher δD_{terr} values reflect warmer summers characterized by D-enriched air masses from the North Atlantic.

5.4. Climate reconstruction

The Sokli sequence is divided into the early, middle and late Eemian phases. Different climatic trends and short-term events can be identified in each phase, based on the integrated interpretation of δD_{terr}, δD_{aq} (this study) and the diatom and pollen data (Plikk et al., 2016; Salonen et al., 2018) (Fig. 7).

5.4.1. Phase I (25.20 m–22.10 m; early Eemian)

The early Eemian is characterized by an early rapid warming trend, followed by a period of increased seasonality and a cooling event towards the end of this phase.

25.20 m–24.90 m; Early Eemian warming trend/deglacial stage. A trend to higher δD_{aq} and δD_{terr} values in the transition from sandy sediments to gyttja marking the onset of the interglacial conditions. The δD_{terr} trend might be further enhanced by the establishment of a forest dominated by birch (Salonen et al., 2018), which tends to produce long chain *n*-alkanes with lower δD values than herbs due to fractionation differences (Yang et al., 2011). In the aquatic ecosystem, the diatom assemblage is dominated by *Cyclotella* spp. (*C. radiosa* and *C. michiganiana*) favored by deep, warm waters and stable summer stratification (Fig. 7) (Plikk et al., 2016). Overall, the diatom community indicates primary production increase reflecting a transition from a deglacial ice-lake with limiting conditions for aquatic production to a more eutrophic lacustrine environment.

24.90 m–23.70 m; Early Eemian/increased seasonality. The δD profiles provide evidence for increased seasonality; low δD_{aq} values reflect cold and prolonged winters dominated by an extensive ice cover and high δD_{terr} values indicate warmer summers. In the catchment, pine forest and mixed boreal forest with spruce (*Picea*) replace the birch forest (Salonen et al., 2018). Both *Pinus* and *Picea* (gymnosperms) tend to fractionate more against deuterium, thus producing long chain *n*-alkanes with lower δD values compared to birch (angiosperms) (Pedentchouk et al., 2008). However, δD_{terr} shows higher values suggesting that any vegetation change likely has a minimal effect in the isotopic variability. The pollen-based T_{jan} generally exhibits a decreasing trend, similar to δD_{aq}, whereas T_{jul} resembles more δD_{terr} (Salonen et al., 2018). The biomarker evidence for seasonality contrast is further corroborated by an increase in the nordic/alpine and benthic diatom species, i.e. *Fragilaria*, indicating lower water temperatures and short mixing periods likely as a result of a pronounced seasonality with long cold winters and short warm summers (Fig. 7) (Plikk et al., 2016). However, lake conditions become more eutrophic with slightly prolonged spring indicated by an increase in the spring diatom bloom of *Stephanodiscus* species, green algae, and the aquatic plant, *Myriophyllum spicatum*, which gradually dominate the summer stratification (Plikk et al., 2016).

23.70 m–22.10 m; tunturi cooling-drying event. The δD_{aq} and δD_{terr} records exhibit a trend towards lower values marking the onset of a major climate perturbation. This event was first defined on the basis of the terrestrial record where the boreal forest is replaced by sub-arctic, open birch–pine forest leading to a T_{jul} drop in the order of 2–4 °C (Tunturi cooling event; 23.45 m–22.55 m) (Helmens et al., 2015; Salonen et al., 2018). Overall, diatoms (increase in *Aulacoseira*) and pollen depict colder, more open, arid and wind stress environment with a brief return to milder conditions through the event (23.00 m–22.80 m). The biomarker δD records, however, show an earlier cooling trend from ca. 23.70 m coinciding with an increase in cold water-oligotrophic green algae before the strong response in the terrestrial record (Fig. 7). In addition, the δD_{terr} record exhibits more pronounced lower values near the end of the event, between 22.50 m and 22.30 m, when the pollen data show a warming trend. It is possible that δD_{terr} might be enhanced by changes in the vegetation in this part of the sequence where pine forest replaces the birch–pine forest.

5.4.2. Phase II (22.10 m–17.50 m; middle Eemian)

This phase represents the mid-climatic optimum conditions divided into an early warming trend and a late period of decreased seasonality with cooler summers.

22.10 m–19.60 m; main climatic optimum conditions. The δD_{aq} and δD_{terr} profiles reach higher values; the same applies to T_{jul} indicating that the climate was ca. 3 °C warmer than today. The diatom assemblage reflects the development of a highly productive lake with extended mixing periods and a prolonged growing season mainly as an effect of milder winters and an earlier ice-out; conditions favorable to the spring bloom dominated by *Stephanodiscus species* (Fig. 7) (Plikk et al., 2016). However, towards the middle part of this phase (above 20.85 cm), an abrupt shift from *Stephanodiscus* to *Aulacoseira* species indicates shallowing of the lake with an increased mixing regime, leading to a reduced summer thermocline stability (Plikk et al., 2016).

19.60 m–17.50 m; decreased seasonality with colder summers. The δD_{aq} and δD_{terr} records show an interval of lower values, which are more pronounced in δD_{terr}, indicating decreased seasonality with cooler summers in agreement with pollen data (Salonen et al., 2018). This trend is followed by a brief return to milder conditions towards the end of the optimum phase. The diatom assemblage is dominated by *Aulacoseira* species reflecting a dimictic and shallow lake with extended mixing period (Plikk et al., 2016). *A.ambigua*, known to require high levels of wind-driven turbulence and light to prosper, reflects strong mixing during late summer (Wang et al., 2008; Plikk et al., 2016). High amounts of *A.ambigua* generally coincide with lower δD_{terr} values (Fig. 7; above 19.60 m), suggesting that cooler summers might be associated with stronger seasonal winds.

5.4.3. Phase III (17.50 m–16.30 m; late Eemian)

This late Eemian phase is characterized by an abrupt cooling event and a period of enhanced climatic instability with an overall cooling trend towards the end of the Eemian.

17.50 m–17.00 m; Värriö cooling event. The δD_{aq} and δD_{terr} records indicate an abrupt cooling event, previously defined by both aquatic and terrestrial proxies (Värriö cooling event) (Plikk et al., 2016; Salonen et al., 2018). In the catchment, trees and shrubs are replaced by herbs and *Sphagnum* (Salonen et al., 2018), which might further lead to even more pronounced trend to lower δD values (Nichols et al., 2010; Taylor et al., 2019). Overall, the pollen data show that T_{jul} dropped by ca 1.5 °C while aquatic proxies indicate a sudden decline in the lake level with colder and less productive conditions as well as more extensive ice cover (Fig. 7; peaks in *Fragilariacaea/Staurosirella pinnata* and *Pediastrum integrum*) (Plikk et al., 2016).

17.00 m–16.30 m; climatic instability/cooling trend. Following the Värriö event, δD_{aq} and δD_{terr} exhibit a small recovery phase coinciding with rising T_{jul} values. This warming is succeeded by a decline δD trend and a slightly cooling trend in T_{jul} as herbs and birch forest return to the area (Salonen et al., 2018). Overall, the biomarker signal is paralleled by changes in the diatom community and other green algae reflecting two stages in the late Eemian development of the lake: (i) a return to littoral, overgrowing and eutrophic conditions with a subtle increase in water level (peak in *A. ambigua*), and finally (ii) an unstable environment with further decreasing water level, and cooler and less productive conditions (Plikk et al., 2016).

6. Discussion

6.1. Effects of teleconnection indices

The Eemian climate was influenced by substantial changes in the latitudinal, annual and seasonal insolation cycle, attributed to shifts in the orbital configuration leading to a warmer climate state with pronounced high-northern latitude warming (Pedersen et al., 2016). The climate system response to this orbital forcing was accompanied by a variety of feedback mechanisms that caused a modification of atmospheric circulation patterns leading to regional climate changes both spatially and temporally.

In our study, the δD profiles plotted against age generally follow the long-term trends of secular seasonal insolation forcing in the northern high latitudes during the Eemian (Fig. 8) (Berger and Loutre, 1991). They also exhibit high frequency variability on centennial to millennial scales (Fig. 8). Both the short-term and the long-term δD trends are interpreted to reflect changes in the temperature and moisture source and, consequently, in the relative dominance of various atmospheric circulation patterns as a response to orbital forcings and feedback mechanisms (Cruz et al., 2005). The Sokli site is located in the transitional zone between the oceanic climate of Western Europe, the continental climatic sectors of Siberia and the polar climate. Therefore, the δD variability can be largely attributed to changes between continentality/polar and oceanic influence associated with shifts from a western to eastern zonal flow and/or meridional flow and vice versa. These changes can be connected to the modes of North Atlantic Oscillation (NAO) and Arctic Oscillation (AO) reflecting the strengths of the westerlies and the polar vortex, respectively, as well as to the intensity of the Siberian High.

Our data indicate that the transition into the Eemian is characterized by a broad -scale change in the atmospheric circulation systems associated with the dominance of more D-enriched-westerly-derived air masses over the study area. Other records across Europe indicate abrupt shifts from a continental to an oceanic climate regime with stronger westerlies leading to warmer and wetter conditions (Cheddadi et al., 1998; Klotz et al., 2003; Brewer et al., 2008; Wilcox et al., 2020).

An outstanding feature of the Sokli proxy integration is the distinct seasonality contrast and the cooling events in the early and late Eemian, which interrupt the overall warming trend. An increased seasonality contrast is indicated by the pollen data from the central Europe during the early Eemian (Brewer et al., 2008), and coincides with an increased summer insolation and decreased winter insolation (Berger and Loutre, 1991). The response of the atmospheric circulation to the Arctic sea ice loss had likely an impact on the seasonality contrast: sea ice concentrations in the early Eemian were distinctly lower especially during the summers and autumns (Stein et al., 2017). Model simulations and studies of reanalysis data have shown that anomalously low sea ice in Barents-Kara Seas during autumn tends to induce an amplification of the Siberian High as well as a negative phase of NAO–AO through weakening of the stratospheric polar vortex leading to a meridional flow and anomalously cold Eurasian winters (Honda et al., 2009, Kim et al., 2014; Petrie et al., 2015 and references there in). The strengthening of the Siberian High for the early Eemian is likely reflected by the low $\delta^{18}O$ diatom values from Lake Baikal in eastern Siberia resulting in a more continental and/or polar climate pattern (Fig. 8) (Mackay et al., 2013). In addition, isotopic and faunal data from the Bahamas in the tropical Atlantic reveal a northward displacement of the Intertropical Convergence Zone (ITCZ) (Fig. 8) (Zhuravleva and Bauch, 2018). This would strengthen the blocking effects of the Subtropical High over western and central Europe during the summer attracting warm air masses from the southwest that would enhance subsidence and surface heating (Davis et al., 1996). In connection to the effects of the Subtropical High, annual to inter-annual variations in summer temperatures in Northern Finland are best explained by the East Atlantic (EA) pattern (Fig. 1) (Irannezhad et al., 2015). Its positive phase is characterized by a negative pressure anomaly west of the British Isles leading to a warm airflow (southwesterly wind) over Europe and above-average summer temperatures (Wulff et al., 2017).

The subsequent Tunturi cooling event in Sokli is prominently observed in records from the North Atlantic and Europe as dry and cold conditions (Fig. 8) (Lauritzen, 1995; Rioual et al., 2001; Brewer et al., 2008; Tzedakis et al., 2018; Finné et al., 2019). However, the exact timing if this event varies from site to site being centered at 126.2 ka BP in the Korallgrottan cave record in NW Sweden (Finné et al., 2019) and at 125.5 ± 0.5 ka BP in the Swiss Alps (Wilcox et al., 2020). Overall, this climatic perturbation occurs at around the same time as the maximum summer insolation and minimum winter insolation coinciding with an increase in ice-rafted debris (IRD), lower sea surface temperatures (SSTs) and a small increase in the ice volume in the North Atlantic (Fig. 8) (Berger and Loutre, 1991; McManus et al., 2002; Oppo et al., 2006, 2007; Irvali et al. 2012). It has been suggested that the melting of the Greenland ice sheet or residual ice masses from the Laurentide ice sheet led to the slow-down of the Atlantic meridional overturning circulation (AMOC) (Galaasen et al., 2014; Zhuravleva et al., 2017). The $\delta^{18}O$ diatom values from Lake Baikal indicate a stronger Siberia High leading to a more continental climate (Fig. 8) (Mackay et al., 2013). In addition, an abrupt southern displacement of the ITCZ is evident in the tropical Atlantic (Fig. 8) (Zhuravleva and Bauch, 2018). This would result in a weaker Subtropical High and more negative EA phases during summers, characterized by a positive pressure anomaly over W-NW Atlantic causing a cold air advection and below-average temperatures (Irannezhad et al., 2015; Wulff et al., 2017). These features of the Tunturi event have many parallels with the Younger Dryas event just before the start of the Holocene.

The Eemian optimum phase in the Sokli record at ca. 126–124 ka BP coincides with a warming trend in records from Norway, Sweden and Greenland within the range of dating uncertainties (Fig. 8) (Lauritzen, 1995; NEEM, 2013; Finné et al., 2019). Other records

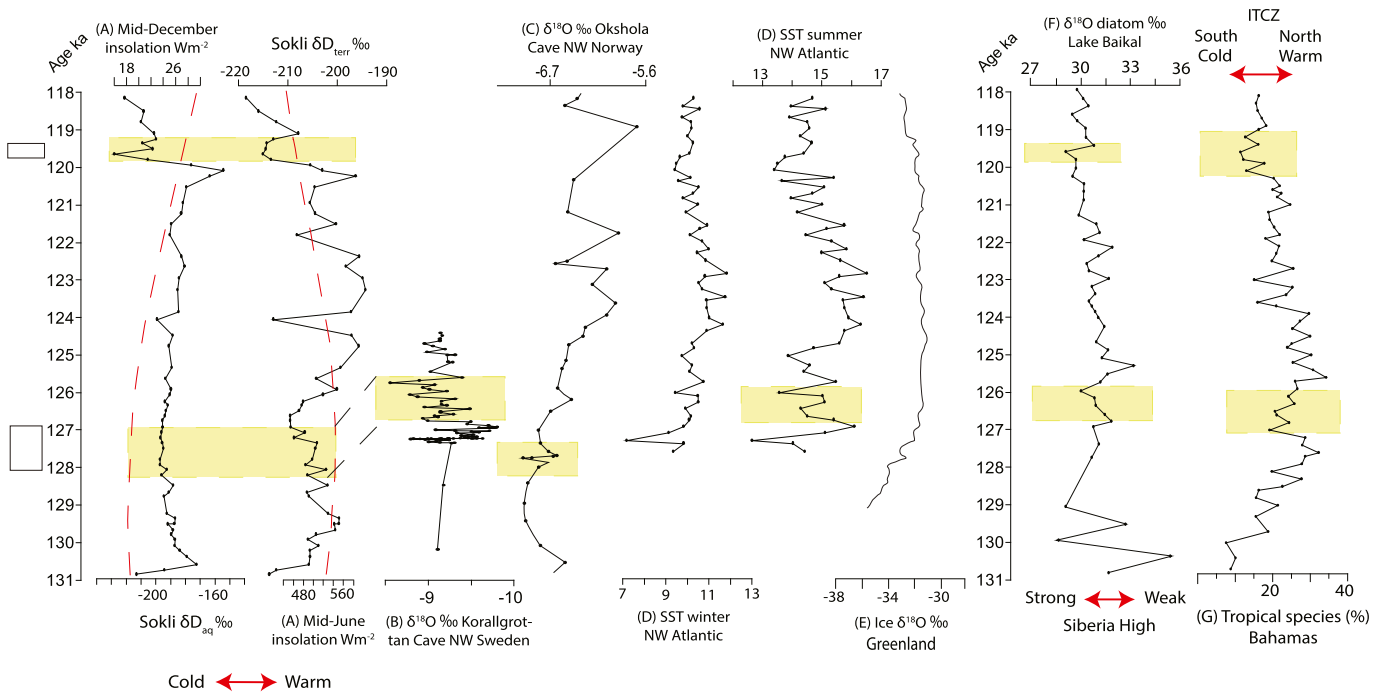

Fig. 8. Comparison of the Sokl δD records with other regional and global records and climate forcing series: (A) Sokl δD records plotted together with December and June insolation at 60°N, (B) Korallgrottan Cave δ18O, NW Sweden (Finné et al., 2019), (C) Okshola Cave $\delta^{18}O$, NW Norway (Lauritzen, 1995), (D) SST estimates derived from modern analog technique from ODP Site 980, WNW Atlantic (Oppo et al., 2007), (E) Ice $\delta^{18}O$ records from NEEM ice cores from Greenland (NEEM community members, 2013), (F) $\delta^{18}O$ diatom profile from Lake Baikal reflecting shifts in the Siberia High intensity (Mackay et al., 2013) and (G) Relative abundances of the tropical species *G. sacculifer* and *G. ruber* in core MD99-2202, Bahamian archipelago associated with shifts in the Intertropical Convergence Zone (ITCZ) during the Eemian (Zhuravleva and Bauch, 2018). The coloured bars indicate the Tunturi and Värriö cooling events in our record, and their suggested counterparts in other datasets.

from central Europe indicate the dominance of more stable conditions (Dabkowski et al., 2016) with an increase in mean annual temperatures and precipitations culminating at ca. 124 ka BP (Vansteenberge et al., 2016; Wilcox et al., 2020). A substantial increase in winter temperatures is observed in the southern part of the East European Plain during the optimum phase (Velichko et al., 2017), coinciding with an increase in North Atlantic SSTs (Fig. 8) (Oppo et al., 2006, 2007), stronger AMOC (Salonen et al., 2018 and references therein) and the lowest global ice volume (Kukla et al., 2002). The Lake Baikal record reveals a weaker Siberian High (Fig. 8) (Mackay et al., 2013), compensated by stronger westerlies/zonal flow with frequent incursions of the Atlantic air to the east, that is, a shift from NAO^- to NAO^+ in the North Atlantic. A dominant zonal flow would then cause warmer and wetter conditions during the optimum phase. This change in atmospheric circulation systems could be related to the increasing winter insolation (Berger and Loutre, 1991) that would trigger large temperature differences between the mid- and high latitudes leading to the development of large latitudinal pressure gradients (Li et al., 2019).

The Eemian thermal maximum in Sokli was interrupted by a period of decreased seasonality with colder summers in agreement with a cooling trend in western and central Europe from ca. 124 ka BP (Brewer et al., 2008; Dabkowski et al., 2016; Wilcox et al., 2020). The Sokli δD record resembles the declining trend in the Baikal record reflecting a more continental climate between ca. 123 and 121 ka (Fig. 8) (Mackay et al., 2013). This coincides with a cooling trend in the North Atlantic, especially in the summer SSTs, coupled with a southward displacement of ITCZ, leading to a weaker Subtropical High and a more negative EA pattern (Fig. 8) (Oppo et al., 2006, 2007; Zhuravleva and Bauch, 2018). The middle Eemian is also characterized by a further reduction in the Arctic sea ice during summers (Stein et al., 2017). In model simulations, Arctic sea ice loss during early summer is related to a negative summer NAO and equatorward shift of the eddy-driven jet because of a reduction in the meridional temperature gradients (Knudsen et al., 2015; Petrie et al., 2015). This is in agreement with the Sokli δD record as negative summer NAO would result in colder conditions in northern Europe associated with stronger northerly winds and moisture transport from the Arctic (Folland et al., 2009).

The Late Eemian in Sokli starts with an abrupt cooling (Värriö event), corresponding to a reduced summer insolation (Fig. 8) (Berger and Loutre, 1991). During this period, there is further evidence for strengthening of the Siberia High (Mackay et al., 2013), lower SSTs in the North Atlantic (Oppo et al., 2006, 2007), and an abrupt southward displacement of the ITCZ and the Subtropical High (Fig. 8) (Zhuravleva and Bauch, 2018). A similar event identified in the North Atlantic and East Greenland at ca. 117 ka, was attributed to an increasing southward incursion of Arctic waters leading to a slowdown of AMOC and a southern position of the polar front (Mokeddem et al., 2014; Zhuravleva et al., 2017).

The transition into glacial conditions towards the end of the Eemian is slower than the onset of the inter-glacial period, which is a typical feature of Glacial-Interglacial climate dynamics. The Sokli data indicate an enhanced climatic instability and an overall cooling trend in agreement with pollen records from northern Europe (Brewer et al., 2008). The $\delta^{18}O$ diatom values from Lake Baikal reflect a fluctuating transition to a continental climate coupled with a further southward displacement of the ITCZ and the associated Subtropical High (Fig. 8) (Mackay et al., 2013; Zhuravleva and Bauch, 2018).

The late Eemian summer cooling is attributed to a decreased summer insolation leading to changes in atmospheric patterns. However, the winter insolation shows an increasing trend. This is not apparent from Sokli δD_{aq}, where decreasing values also indicate

cooling. In some model simulations, winter temperatures at 60–90 °N exhibit similar trends as Sokli δD_{aq} which could be explained by various feedback mechanisms counteracting the positive forcing of winter insolation (Bakker et al., 2013). One possibility is that lower summer temperatures, along with an increased northward moisture transport, led to longer sea-ice and snow cover, which acted as a feedback to enhance cooling (Khodri et al., 2001). In addition, high precipitation amounts could have resulted in an increase in the freshwater runoff into the Arctic Ocean causing a southward extension of the cold and less-salty water at the expense of the northward extension of warmer waters reducing the thermohaline circulation (Khodri et al., 2001; Crucifix and Loutre, 2002). This would be consistent with a sea surface cooling observed in the western Nordic Seas and the Labrador Sea (Van Nieuwenhove et al., 2013; Irvalı et al., 2016) as well as the gradual decreasing SSTs in the north Atlantic (Fig. 8) (Oppo et al., 2006, 2007).

7. Conclusions

We studied the δD composition of *n*-alkanes in a sediment core from the Sokli site in NE Finland, in order to increase the understanding of seasonal characteristics of interglacial climate dynamics at high latitude during the Eemian period. The δD_{aq} record is interpreted to reflect δD_{lake} variability largely influenced by winter δD_{prec}, ice cover duration and D-depleted meltwater whereas δD_{terr} is mainly influenced by summer δD_{prec} and the evaporation of leaf and soil water. Overall, low δD_{aq} and δD_{terr} values indicate cold conditions associated with the dominance of D-depleted air masses from Arctic and Siberia and higher values reflect a warm climate dominated by D-enriched westerly air masses. Three phases of major climatic changes can be identified in Sokli that follow the secular variations in seasonal insolation: (i) an early interglacial rapid warming succeeded by a period of strong seasonality, (ii) a mid-climatic optimum phase with gradually decreased seasonality and cooler summers, and (iii) climatic instability in the latest phase with an overall cooling trend. Superimposed on this trend, two abrupt cooling events occur in the early (Tunturi event) and late Eemian (Värriö event).

The prolonged and cold winters during the early Eemian coincide with reduced winter insolation and anomalously low sea ice in Barents-Kara Seas that would induce an amplification of the Siberian high and negative NAO–AO phases. A shift to an oceanic climate during the mid-Eemian phase corresponds to gradually increased winter insolation that would lead to a large latitudinal temperature and pressure gradient causing stronger westerlies and positive NAO. Summer atmospheric circulation patterns have also influenced the δD_{terr} record. Warm (cold) summers during the early (late) Eemian generally coincide with maximum (minimum) June insolation and northward (southward) displacement of ITCZ and expansion (retreat) of Subtropical High over Europe. The cooling events in the early and late Eemian can be linked to disturbances in the North Atlantic Ocean circulation.

Our study complements the scarcely available Eemian proxy data from high-latitude continental regions and especially corroborates the seasonal signal, which has remained poorly constrained. In future studies, the Sokli data can be used as a reference for climate modeling to further understand Interglacial climate dynamics, which in turn can help to improve projections of future warming.

Author contributions

Christos Katrantsiotis performed the quantification and compound-specific isotope analysis of *n*-alkanes, made the interpretation and wrote the paper with important inputs from all co-authors.

Research dataset

The dataset are in the following repository: https://bolin.su.se/data/katrantsiotis-2021-sokli-1.

Declaration of competing interest

The authors declare that they have no known competing financial interests or personal relationships that could have appeared to influence the work reported in this paper.

Acknowledgements

This research was primarily financed by the Bolin Center for Climate Research, Stockholm University. KFH further acknowledges funding from Swedish Nuclear Fuel and Waste Management Company (SKB); JSS from the Academy of Finland (project 1310649). We acknowledge Anna Hägglund in particular for assistance while operating the GC-IRMS, Klara Hajnal with the assistance of extracting *n*-alkanes and the preparations of samples for bulk isotope analysis and Heike Siegmund for the assistance of bulk isotope analysis at the Stable Isotope Laboratory at Stockholm University.

Appendix A. Supplementary data

Supplementary data to this article can be found online at https://doi.org/10.1016/j.quascirev.2021.107250.

References

Aichner, B., Feakins, S.J., Lee, J.E., Herzschuh, U., Liu, X., 2015. High resolution leaf wax carbon and hydrogen isotopic record of late Holocene paleoclimate in arid Central Asia. Clim. Past 11, 619–633.

Aichner, B., Ott, F., Slowinski, M., Noryskievicz, A.M., Brauer, A., Sashce, D., 2018. Leaf wax n-alkane distributions record ecological changes during Younger Dryas at Trzechowskie paleolake (northern Poland) without temporal delay. Clim. Past 14, 1607–1624.

Alexanderson, H., Eskola, K.O., Helmens, K.F., 2008. Optical dating of a late Quaternary sediment sequence from Sokli, northern Finland. Geochronometria 32, 51–59.

Autio, J., Heikkinen, O., 2002. The climate of northern Finland. Fennia Int. J. Geograp. 180 (1–2), 61–66.

Bakker, P., Stone, E.J., Charbit, S., Groger, M., Krebs-Kanzow, U., Ritz, S.P., Varma, V., Khon, V., Lunt, D.J., Mikolajewicz, U., Prange, M., Renssen, H., Schneider, B., Schulz, M., 2013. Last interglacial temperature evolution – a model intercomparison. Clim. Past 9 (2), 605–619.

Bakker, P., Masson-Delmotte, V., Martrat, B., Charbit, S., Renssen, H., Gröger, M., Krebs-Kanzow, U., Lohmann, G., Lunt, D.J., Pfeiffer, M., Phipps, S.J., Prange, M., Ritz, S.P., Schulz, M., Stenni, B., Stone, E.J., Varma, V., 2014. Temperature trends during the Present and Last Interglacial periods – a multi-model-data comparison. Quat. Sci. Rev. 99, 224–243.

Berger, A., Loutre, M.F., 1991. Insolation values for the climate of the last 10 million years. Quat. Sci. Rev. 10, 297–317.

Bliedtner, M., Schäfer, I.K., Zech, R., von Suchodoletz, H., 2018. Leaf wax n-alkanes in modern plants and top soils from eastern Georgia (Caucasus) – implications for reconstructing regional paleovegetation. Biogeosciences 15, 3927–3936.

Blokker, P., Schouten, S., van den Ende, H., de Leeuw, J.W., Hatcher, P.G., Sinninghe Damsté, J.S., 1998. Chemical structure of algaenans from the fresh water algae *Tetraedron minimum, Scenedesmus communis* and *Pediastrum boryanum*. Org. Geochem. 29, 1453–1468.

Bonne, J.-L., Meyer, H., Behrens, M., Boike, J., Kipfstuhl, S., Rabe, B., Schmidt, T., Schönicke, L., Steen-Larsen, H.C., Werner, M., 2020. Moisture origin as a driver of temporal variabilities of the water vapour isotopic composition in the Lena River Delta, Siberia. Atmos. Chem. Phys. 20, 10493–10511.

Brewer, S., Guiot, J., Sánchez-Goñi, M.F., Klotz, S., 2008. The climate in Europe during the Eemian: a multi-method approach using pollen data. Quat. Sci. Rev. 27, 2303–2315.

Bush, R.T., McInerney, F.A., 2013. Leaf wax n-alkane distributions in and across modern plants: implications for paleoecology and chemotaxonomy. Geochem. Cosmochim. Acta 117, 161–179.

CAPE-Last Interglacial Project Members, 2006. Last Interglacial Arctic warmth confirms polar amplification of climate change. Quat. Sci. Rev. 25, 1383–1400.

Cheddadi, R., Mamakova, K., Guiot, J., de Beaulieu, J.-L., Reille, M., Andrieu, V., Granoszewski, W., Peyron, O., 1998. Was the climate of the Eemian stable? A quantitative climate reconstruction from seven European pollen records. Palaeogeogr. Palaeoclimatol. Palaeoecol. 143, 73–85.
Crucifix, M., Loutre, M.-F., 2002. Transient simulations over the last interglacial period (126- 7 115 kyr BP): feedback and forcing analysis. Clim. Dynam. 19, 417–433.
Cruz Jr., F.W., Burns, S.J., Karmann, I., Sharp, W.D., Vuille, M., Cardoso, A.O., Ferrari, J.A., Silva Dias, P.L., Vlana Jr., O., 2005. Insolation-driven changes in atmospheric circulation over the past 116,000 years in subtropical Brazil. Nature 434, 63–66.
Curtin, L., D'Andrea, W.J., Balascio, N.L., Pugsley, G., de Wet, G., Bradley, R., 2019. Holocene and Last Interglacial climate of the Faroe Islands from sedimentary plant wax hydrogen and carbon isotopes. Quat. Sci. Rev. 223, 105930.
Dabkowski, J., Limondin-Lozouet, N., Anders, J., Marca-Bell, A., Antoine, P., 2016. Climatic and environmental variations during the last interglacial recorded in a northern France tufa (caours, somme basin). Comparisons with regional to global records. Quaternaire 27, 249–261.
Dansgaard, W., 1964. Stable isotopes in precipitation. Tellus 16, 436–468.
Davis, R.E., Hayden, B.P., Gay, D.A., Philips, W.L., Jones, G.V., 1996. the North atlantic subtropical anticyclone. J. Clim. 10, 728–744.
Demény, A., Kern, Z., Czuppon, G., Németh, A., Leél-Őssy, S., Siklósy, Z., Lin, K., Hu, H.M., Shen, C.C., Vennemann, T.W., Haszpra, L., 2017. Stable isotope compositions of speleothems from the last interglacial – spatial patterns of climate fluctuations in Europe. Quat. Sci. Rev. 161, 68–80.
Diefendorf, A.F., Freeman, K.H., Wing, S.L., Graham, H.V., 2011. Production of n-alkyl lipids in living plants and implications for the geologic past. Geochem. Cosmochim. Acta 75 (23), 7472–7485.
Drysdale, R.N., Zanchetta, G., Hellstrom, J.C., Fallick, A.E., Zhao, J.X., 2005. Stalagmite evidence for the onset of the Last Interglacial in southern Europe at 129 1 ka. Geophys. Res. Lett. 32, L24708.
Duan, Y., Wu, B., Xu, L., He, J., Sun, T., 2011. Characterisation of n-alkanes and their hydrogen isotopic composition in sediments from Lake Qinghai, China. Org. Geochem. 42, 720–726.
Ficken, K.J., Li, B., Swain, D.L., Eglinton, G., 2000. An n-alkane proxy for the sedimentary input of submerged/floating freshwater aquatic macrophytes. Org. Geochem. 31, 745–749.
Field, M.H., Huntley, B., Muller, H., 1994. Eemian climate fluctuations observed in a European pollen record. Nature 371, 779–783.
Finné, M., Salonen, J.S., Frank, N., Helmens, K.F., Schröder-Ritzrau, A., Deininger, M., Holzkämper, S., 2019. Last interglacial climate in northern Sweden—insights from a speleothem record. Quaternary 2 (3), 29.
Fischer, H., Meissner, K.J., Mix, A.C., et al., 2018. Palaeoclimate constraints on the impact of 2 °C anthropogenic warming and beyond. Nat. Geosci. 11, 474–485.
Folland, C.K., Knight, J., Linderholm, H.W., Fereday, D., Ineson, S., Hurrell, J.W., 2009. The summer north Atlantic oscillation: past, present, and future. J. Clim. 22, 1082–1103.
France, R.L., 1995. Carbon-13 enrichment in benthic compared to planktonic algae: foodweb implications. Mar. Ecol. Prog. Ser. 124, 307–312.
Francis, D.R., Wolfe, A.P., Walker, I.R., Miller, G.H., 2006. Interglacial and Holocene temperature reconstructions based on midge remains in sediments of two lakes from Baffin Island, Nunavut, Arctic Canada. Palaeogeogr. Palaeoclimatol. Palaeoecol. 236 (1–2), 107–124.
Galaasen, E.V., Ninnemann, U.S., Irvali, N., Kleiven, H.F., Rosenthal, Y., Kissel, C., Hodell, D.A., 2014. Rapid reductions in north atlantic deep water during the peak of the last interglacial period. Science 343, 1129–1132.
Goldsmith, Y., Polissar, P.J., deMenocal, P.B., Broecker, W.S., 2019. Leaf wax δD and $\delta^{13}C$ in soils record hydrological and environmental information across a climatic gradient in Israel. J. Geophys. Res.: Biogeosciences 124, 2898–2916.
Guenther, F., Aichner, B., Siegwolf, R., Xu, B., Yao, T., Gleixner, G., 2013. A synthesis of hydrogen isotope variability and its hydrological significance at the Qinghai-Tibetan Plateau. Quat. Int. 313– 314, 3–16.
Helmens, K.F., 2014. The Last Interglacial-Glacial cycle (MIS 5e2) re-examined based on long proxy records from central and northern Europe. Quat. Sci. Rev. 86, 115–143.
Helmens, K.F., Räsänen, M.E., Johansson, P.W., Jungner, H., Korjonen, K., 2000. The last interglacial-glacial cycle in NE Fennoscandia: a nearly continuous record from Sokli (Finnish Lapland). Quat. Sci. Rev. 19, 1605–1623.
Helmens, K.F., Johansson, P.W., Räsänen, M.E., Alexanderson, H., Eskola, K.O., 2007. Ice-free intervals at Sokli continuing into marine isotope stage 3 in the central area of the scandinavian glaciations. Geol. Survey Finland 79, 17–39.
Helmens, K.F., Salonen, J.S., Plikk, A., Engels, S., Väliranta, M., Kylander, M., Brendryen, J., Renssen, H., 2015. Major cooling intersecting peak Eemian interglacial warmth in northern Europe. Quat. Sci. Rev. 122, 293–299.
Honda, M., Inoue, J., Yamane, S., 2009. Influence of low Arctic sea-ice minima on anomalously cold Eurasian winters. Geophys. Res. Lett. 36, L08707.
Huang, W., Wang, B., Wright, J.S., Chen, R., 2016. On the non-stationary relationship between the siberian high and arctic oscillation. PLoS One 11 (6), e0158122.
IAEA, International Atomic Energy Agency, 2020. Global Network of Isotopes in Precipitation Database. http://nucleus.iaea.org. (Accessed 5 August 2020).
Ilvonen, E., 1973. Eem - kerrostuma savukosken soklilla. Julkaisija: Suomen Geologinen Seura 25, 81–84.
Ionita, M., 2014. The impact of the east atlantic/western Russia pattern on the hydroclimatology of Europe from mid-winter to late spring. Climate 2, 296–309.
IPCC, 2018. Special report on global warming of 1.5°C above pre-industrial levels and related global greenhouse gas emission pathways. Available online at: https://www.ipcc.ch/sr15/.
IPCC, 2021. Climate Change 2021: the Physical Science Basis. Contribution of Working Group I to the Sixth Assessment Report of the Intergovernmental Panel on Climate Change. Cambridge University Press (in press).
Irannezhad, M., Marttila, H., Kløve, B., 2014. Long-term variations and trends in precipitation in Finland. Int. J. Climatol. 34, 3139–3153.
Irannezhad, M., Chen, D., Kløve, B., 2015. Interannual variations and trends in surface air temperature in Finland in relation to atmospheric circulation patterns, 1961–2011. Int. J. Climatol. 35, 3078–3092.
Irannezhad, M., Marttila, H., Chen, D., Kløve, B., 2016. Century-long variability and trends in daily precipitation characteristics at three Finnish stations. Adv. Clim. Change Res. 7, 54–69.
Irvalı, N., Ninnemann, U.S., Galaasen, E.V., Rosenthal, Y., Kroon, D., Oppo, D.W., Kleiven, H.F., Darling, K.F., Kissel, C., 2012. Rapid switches in subpolar North Atlantic hydrography and climate during the Last Interglacial (MIS 5e). Paleoceanography 27, PA2207.
Irvalı, N., Ninnemann, U.S., Kleiven, H., Kikki, F., Galaasen, E.V., Morley, A., Rosenthal, Y., 2016. Evidence for regional cooling, frontal advances, and East Greenland Ice Sheet changes during the demise of the last interglacial. Quat. Sci. Rev. 150, 184–199.
Jansen, E., Overpeck, J., Briffa, K.R., Duplessy, J.-C., Joos, F., Masson-Delmotte, V., Olago, D., Otto-Bliesner, B., Peltier, W.R., Rahmstorf, S., Ramesh, R., Raynaud, D., Rind, D., Solomina, O., Villalba, R., Zhang, D., 2007. Palaeoclimate. In: Solomon, S., Qin, D., Manning, M., Chen, Z., Marquis, M., Averyt, K.B., Tignor, M., Miller, H.L. (Eds.), Climate Change 2007: the Physical Science Basis. Contribution of Working Group I to the Fourth Assessment Report of the Intergovernmental Panel on Climate Change. Cambridge University Press, Cambridge, UK, pp. 433–497.
Järvenoja, S., 2005. Arctic Oscillation and its Impact on Finland's Climate: XXII Geophysical Days. May 19–20, 2005, Helsinki.
Jonsson, C.E., Leng, M.J., Rosqvist, G.C., Seibert, J., Arrowsmith, C., 2009. Stable oxygen and hydrogen isotopes in sub-Arctic lake waters from northern Sweden. J. Hydrol. 376 (1–2), 143–151.
Kahmen, A., Schefuß, E., Sachse, D., 2013. Leaf water deuterium enrichment shapes leaf wax n-alkane δD values of angiosperm plants I: experimental evidence and mechanistic insights. Geochem. Cosmochim. Acta 111, 39–49.
Katrantsiotis, C., Kylander, M., Smittenberg, R., Yamoah, K.K.A., Hättestrand, M., Avramidis, P., Strandberg, N.A., Norström, E., 2018. Eastern Mediterranean hydroclimate reconstruction over the last 3600 years based on sedimentary n-alkanes, their carbon and hydrogen isotope composition and XRF data from the Gialova Lagoon, SW Greece. Quat. Sci. Rev. 194, 77–93.
Katrantsiotis, C., Norström, E., Smittenberg, R., Finné, M., Weiberg, W., Hättestrand, M., Avramidis, P., Wastegård, S., 2019. Climate changes in the Eastern Mediterranean over the last 5000 years and their links to the high-latitude atmospheric patterns and Asian monsoons. Global Planet. Change 175, 36–51.
Khodri, M., Leclainche, Y., Ramstein, G., Braconnot, P., Marti, O., Cortijo, E., 2001. Simulating the amplification of orbital forcing by ocean feedbacks in the last glaciation. Nature 410, 570–574.
Kim, B.-K., Son, S.-W., Min, S.-K., Jeong, J.-H., Kim, S.-J., Zhang, X., Shim, T., Yoon, J.-H., 2014. Weakening of the stratospheric polar vortex by Arctic sea-ice loss. Nat. Commun. 5, 4646.
Kjellman, S.E., Schomacker, A., Thomas, E.K., Håkansson, L., Duboscq, S., Cluett, A.A., Farnsworth, W.R., Allaart, L., Cowling, O.C., McKay, N.P., Brynjólfsson, S., Ingolfsson, O., 2020. Holocene precipitation seasonality in northern Svalbard: influence of sea ice and regional ocean surface conditions. Quat. Sci. Rev. 240, 106388.
Klotz, S., Guiot, J., Mosbrugger, V., 2003. Continental European Eemian and early Würmian climate evolution: comparing signals using different quantitative reconstruction approaches based on pollen. Global Planet. Change 36, 277–294.
Knudsen, E.M., Orsolini, Y.J., Furevik, T., Hodges, K.I., 2015. Observed anomalous atmospheric patterns in summers of unusual Arctic sea ice melt. J. Geophys. Res.: Atmosphere 120, 2595–2611.
Kortelainen, N.M., Karhu, A.K., 2004. Regional and seasonal trends in the oxygen and hydrogen isotope ratios of Finnish groundwaters: a key for mean annual precipitation. J. Hydrol. 285 (1–4), 143–157.
Kukla, G.J., Bender, M.L., de Beaulieu, J.-L., Bond, G., Broecker, W.S., Cleveringa, P., Gavin, J.E., Herbert, T.D., Imbrie, J., Jouzel, J., Keigwin, L.D., Knudsen, K.-L., McManus, J.F., Merkt, J., Muhs, D.R., Müller, H., Poore, R.Z., Porter, S.C., Seret, G., Shackleton, N.J., Turner, C., Tzedakis, P.C., Winograd, I.J., 2002. Last interglacial climates. Quat. Res. 58, 2–13.
Kyllönen, K., 2018. The variation of stable isotopes of water in precipitation in Finland. Master Thesis. University of Oulu.
Landais, A., Masson-Delmotte, V., Capron, E., Langebroek, P.M., Bakker, P., Stone, E.J., Merz, N., Raible, C.C., Fischer, H., Orsi, A., Prié, F., Vinther, B., Dahl-Jensen, D., 2006. How warm was Greenland during the last interglacial period? Clim. Past 12, 1933–1948.
Lauritzen, S.-E., 1995. High-Resolution paleotemperature proxy record for the last interglaciation based on Norwegian speleothems. Quat. Res. 43 (2), 133–146.
Lee, D.Y., Lin, W., Petersen, M.R., 2020. Wintertime arctic oscillation and north atlantic oscillation and their impacts on the northern hemisphere climate in E3SM. Clim. Dynam. 55, 1105–1124.
Li, Y., Song, Y., Yin, Q., Han, L., Wang, Y., 2019. Orbital and millennial northern mid-

latitude westerlies over the last glacial period. Clim. Dynam. 53, 3315–3324.
Liu, H., Liu, W., 2016. n-Alkane distributions and concentrations in algae, submerged plants and terrestrial plants from the Qinghai-Tibetan Plateau. Organic Geochemistrey 99, 10–22.
MacCracken, M.C., Kutzbach, J., 1991. Comparing and contrasting Holocene and Eemian warm periods with greenhouse-gas-induced warming. Dev. Atmos. Sci. 19, 17–33.
Mackay, A.W., Swann, G.E.A., Fagel, N., Fietz, S., Leng, M.J., Morley, D., Rioual, P., Tarasov, P., 2013. Hydrological instability during the Last Interglacial in central Asia: a new diatom oxygen isotope record from Lake Baikal. Quat. Sci. Rev. 66, 45–54.
Maslin, M., 2009. Quaternary climate transitions and cycles. In: Gornitz, V. (Ed.), Encyclopedia of Palaeoecology and Ancient Environments. Springer, Dordrecht, pp. 841–855.
McFarlin, J.M., Axford, Y., Masterson, A.L., Osburn, M.R., 2019. Calibration of modern sedimentary δ2H plant wax-water relationships in Greenland lakes. Quat. Sci. Rev. 225, 105978.
McManus, J.F., Oppo, D.W., Keigwin, L.D., Cullen, J.L., Bond, G.C., 2002. Thermohaline circulation and prolonged interglacial warmth in the North Atlantic. Quat. Res. 58, 17–21.
Meyers, P.A., Teranes, J.L., 2001. Sediment organic matter. In: Last, W.M., Smol, J.P. (Eds.), Tracking Environmental Changes Using lake Sediments e Volume II: Physical and Chemical Techniques. Kluwer, Dordrecht, pp. 239–270.
Mikhailova, N.V., Yurovsky, A.V., 2016. The East Atlantic oscillation: mechanism and impact on the European climate in winter. Phys. Oceanogr. 4, 27–36.
Mokeddem, Z., McManus, J.F., Oppo, D.W., 2014. Oceanographic dynamics and the end of the last interglacial in the subpolar North Atlantic. Proc. Natl. Acad. Sci. U. S. A 111, 11263–11268.
NEEM community members, 2013. Eemian interglacial reconstructed from a Greenland folded ice core. Nature 493, 489–494.
Nichols, J.E., Booth, R.K., Jackson, S.T., Pendall, E.G., Huang, Y., 2010. Differential hydrogen isotopic ratios of Sphagnum and vascular plant biomarkers in ombrotrophic peatlands as a quantitative proxy for precipitation-evaporation balance. Geochem. Cosmochim. Acta 74, 1407–1416.
Oppo, D.W., McManus, J.F., Cullen, J.L., 2006. Evolution and demise of the last interglacial warmth in the subpolar north Atlantic. Quat. Sci. Rev. 25, 3268–3277.
Oppo, D.W., McManus, J.F., Cullen, J.L., 2007. Subpolar north Atlantic ODP980 MIS5 sediment data. In: IGBP PAGES/World Data Center for Paleoclimatology, Data Contribution Series # 2007-030. NOAA/NCDC Paleoclimatology Program, Boulder CO, USA.
Paul, C.A., Douglas, M.S.V., Smol, J.P., 2010. Diatom-inferred Holocene climatic and environmental changes in an unusually subsaline high Arctic nunatak pond on Ellesmere Island (Nunavut, Canada). J. Paleolimnol. 44, 913–929.
Pedentchouk, N., Sumner, W., Tipple, B., Pagani, M., 2008. $\delta^{13}C$ and δD compositions of n-alkanes from modern angiosperms and conifers: an experimental set up in central Washington State, USA. Org. Geochem. 39, 1066–1071.
Pedersen, R.A., Langen, P.L., Vinther, B.M., 2016. The last interglacial climate: comparing direct and indirect impacts of insolation changes. Clim. Dynam. 48, 3391–3407.
Petrie, R.E., Shaffrey, L.C., Sutton, R.T., 2015. Atmospheric impact of Arctic sea ice loss in a coupled ocean–atmosphere simulation. J. Clim. 28, 9606–9622.
Plikk, A., Helmens, K.F., Fernández-Fernández, M., Kylander, M., Löwemark, L., Risberg, J., Salonen, J.S., Väliranta, M., Weckström, J., 2016. Development of an Eemian (MIS 5e) Interglacial palaeolake at Sokli (N Finland) inferred using multiple proxies. Palaeogeogr. Palaeoclimatol. Palaeoecol. 63, 11–26.
Plikk, A., Engels, S., Luoto, T.P., Nazarova, L., Salonen, J.S., Helmens, K.F., 2019. Chironomid-based temperature reconstruction for the Eemian Interglacial (MIS 5e) at Sokli, northeast Finland. J. Paleolimnol. 61, 355–371.
Rao, Z., Wu, Y., Zhu, Z., Jia, G., Henderson, A., 2011. Is the maximum carbon number of long1chain *n*-alkanes an indicator of grassland or forest? Evidence from surface soils and modern plants. Chin. Sci. Bull. 56, 1714–1720.
Rioual, P., Andrieu-Ponel, V., Rietti-Shati, M., Battarbee, R.W., de Beaulieu, J.-L., Cheddadi, R., Maurice, R., Svobodova, H., Shemesh, A., 2001. High-resolution record of climate stability in France during the last interglacial period. Nature 413, 293–296.
Rosqvist, G., Jonsson, C., Yam, R., Karlén, W., Shemesh, A., 2004. Diatom oxygen isotopes in pro-glacial lake sediments from northern Sweden: a 5000 year record of atmospheric circulation. Quat. Sci. Rev. 23, 851–859.
Sachs, J.P., Sachse, D., Smittenberg, R.H., Zhang, Z., Battisti, D.S., Golubic, S., 2009. Southward movement of the Pacific intertropical convergence zone AD 1400–1850. Nat. Geosci. 2, 519–525.
Salonen, J.S., Helmens, K.F., Brendryen, J., Kuosmanen, N., Väliranta, M., Goring, S., Korpela, M., Kylander, M., Philip, A., Plikk, A., Renssen, H., Luoto, M., 2018. Abrupt high-latitude climate events and decoupled seasonal trends during the Eemian interglacial. Nat. Commun. 9 (1), 2851.
Schurgers, G., Mikolajewicz, U., Gröger, M., Maier-Reimer, E., Vizcaıno, M., Winguth, A., 2007. The effect of land surface changes on Eemian climate. Clim. Dynam. 29 (4), 357–373.
Stein, R., Fahl, K., Gierz, P., Niessen, F., Lohmann, G., 2017. Arctic Ocean sea ice cover during the penultimate glacial and the last interglacial. Nat. Commun. 8, 373.
Talvitie, J., Lehmuspelto, P., Vuotovesi, T., 1981. Airborne thermal surveying of the groundin Sokli, Finland, geological Survey of Finland. Report of investigation 50, 1–13.
Tanner, B.R., Uhle, M.E., Mora, C.I., Kelley, J.T., Schuneman, P.J., Lane, C.S., Allen, E.S., 2010. Comparison of bulk and compound-specific $\delta^{13}C$ analyses and determination of carbon sources to salt marsh sediments using n-alkane distributions (Maine, USA). Estuarine. Estuarine, Coastal and Shelf Science 86, 283–291.
Taylor, A.K., Benedetti, M.M., Haws, J.A., Lane, C.S., 2019. The hydrogen isotopic compositions of sedimentary mid-chain n-alkanes record ecological change at a Portuguese paleowetland. Quat. Int. 532, 23–33.
Theakstone, W.H., 2011. A seven-year study of oxygen isotopes in daily precipitation at a site close to the Arctic Circle, Tustervatn, Norway: trajectory analysis and links with the North Atlantic Oscillation. Atmos. Environ. 45, 5101–5109.
Thienemann, M., 2017. Reconstructing Holocene Climatic and Environmental Change Using Molecular and Isotopic Proxies from Lake Sedimentary Records. PhD thesis. University of Cologne, Germany.
Throckmorton, H.M., Newman, B.D., Heikoop, J.M., Perkins, G.B., Feng, X., Graham, D.E., O'Malley, D., Vesselinov, V.V., Young, J., Wullschleger, S.D., Wilson, C.J., 2016. Active layer hydrology in an arctic tundra ecosystem: quantifying water sources and cycling using water stable isotopes. Hydrol. Process. 30 (26), 4972–4986.
Tzedakis, P.C., Andrieu, V., de Beaulieu, J.-L., Crowhurst, S., Follieri, M., Hooghiemstra, H., Magri, D., Reille, M., Sadori, L., Shackleton, N.J., Wijmstra, T.A., 1997. Comparison of terrestrial and marine records of changing climate of the last 500,000 years. Earth Planet Sci. Lett. 150, 171–176.
Tzedakis, P.C., Drysdale, R.N., Margari, V., Skinner, L.C., Menviel, L., Rhodes, Rachael H., Taschetto, A.S., Hodell, D.A., Crowhurst, S.J., Hellstrom, J.C., Fallick, A.E., Grimalt, J.O., McManus, J.F., Martrat, B., Mokeddem, Z., Parrenin, F., Regattieri, E., Roe, K., Zanchetta, G., 2018. Enhanced climate instability in the north atlantic and southern Europe during the last interglacial. Nat. Commun. 9, 4235.
Van Nieuwenhove, N., Bauch, H.A., Andruleit, H., 2013. Multiproxy fossil comparison reveals contrasting surface ocean conditions in the western Iceland Sea for the last two interglacials. Palaeogeogr. Palaeoclimatol. Palaeoecol. 370, 247–259.
Vansteenberge, S., Verheyden, S., Cheng, H., Edwards, L.R., Keppens, E., Clayes, P., 2016. Paleoclimate in continental northwestern Europe during the Eemian and Early-Weichselian (125-97 ka): insights from a Belgian speleothem. Clim. Past 12, 1445–1458.
Vartiainen, H., 1980. The Petography, Mineralogy and Petrochemistry of the Sokli Carbonatite Massif, Northern Finland, vol. 313. Geological Survey of Finland, pp. 1–126.
Velichko, A.A., Borisova, O.K., Kononov, YuM., Konstantinov, E.A., Kurbanov, R.N., Morozova, T.D., Panin, P.G., Semenov, V.V., Tesakov, A.S., Timireva, S.N., Titov, V.V., Frolov, P.D., 2017. Reconstruction of Late Pleistocene events in the periglacial area in the southern part of the East European Plain. Dokl. Earth Sci. 475, 895–899.
Wallace, J.M., Gutzler, D.S., 1981. Teleconnections in the geopotential height field during the Northern Hemisphere winter. Mon. Weather Rev. 109, 784–812.
Wang, T., Chen, J., 2020. Long-term trend of precipitation stable isotopic compositions under global warming conditions. J. Radioanal. Nucl. Chem. 325, 557–565.
Wang, X.C., Chen, R.F., Berry, A., 2003. Sources and preservation of organic matter in Plum Island salt marsh sediments (MA, USA): long-chain n-alkanes and stable carbon isotope compositions. Estuar. Coast Shelf Sci. 58, 917–928.
Wang, L., Lu, H., Liu, J., Gu, Z., Mingram, J., Chu, G., Li, J., Rioual, P., Negendank, J.F.W., Han, J., Liu, T., 2008. Diatom-based inference of variations in the strength of Asian winter monsoon winds between 17,500 and 6000 calendar years BP. J. Geophys. Res. 113, D21101.
Wilcox, P.S., Honiat, C., Trüssel, M., Edwards, R.L., Spötl, C., 2020. Exceptional warmth and climate instability occurred in the European Alps during the Last Interglacial period. Communications Earth & Environment 1, 57.
Wulff, C.O., Greatbatch, R.J., Domeisen, D.I.V., Gollan, G., Hansen, F., 2017. Tropical forcing of the summer east Atlantic pattern. Geophys. Res. Lett. 44, 11166–11173.
Yang, H., Liu, W.G., Leng, Q., Hren, M.T., Pagani, M., 2011. Variation in *n*-alkane δD values from terrestrial plants at high latitude: implications for paleoclimate reconstruction. Org. Geochem. 42, 283–288.
Zalat, A., Welc, F., Nitychoruk, J., Marsk, L., Chodyka, M., Zbucki, Ł., 2018. Last two millennia water level changes of the Młynek Lake (Northern Poland) inferred from diatoms and chrysophyte cysts record. Stud. Quat. 35 (2), 77–89.
Zech, M., Buggle, B., Leiber, K., Marković, S., Glaser, B., , Hambach, U., Huwe, B., Stevens, T., Sümegi, P., Wiesenberg, G., Zöller, L., 2009. Reconstructing Quaternary vegetation history in the Carpathian Basin, SE-Europe, using n-alkane biomarkers as molecular fossils: problems and possible solutions, potential and limitations. E Quat. Sci. J. 58 (2), 148–155.
Zhuravleva, A., Bauch, H.A., 2018. Last Interglacial Ocean changes in the Bahamas: climate teleconnections between low and high latitudes. Clim. Past 14 (10), 1361–1375.
Zhuravleva, A., Bauch, H.A., Spielhagen, R.F., 2017. Atlantic water heat transfer through the arctic gateway (fram strait) during the last interglacial. Global Planet. Change 157, 232–243.